

1 **Trisomy 21 induces pericentrosomal crowding disrupting early stages of primary**
2 **ciliogenesis and mouse cerebellar development**

3

4 Cayla E Jewett^{1,2}, Bailey L McCurdy¹, Eileen T O'Toole³, Katherine S Given¹, Carrie H Lin¹,
5 Valerie Olsen¹, Whitney Martin⁴, Laura G Reinholdt⁴, Joaquin M Espinosa^{2,5}, Kelly D Sullivan^{2,6},
6 Wendy B Macklin¹, Rytis Prekeris^{1*}, Chad G Pearson^{1,2*}

7

8 ¹Department of Cell and Developmental Biology, University of Colorado-Anschutz Medical
9 Campus, Aurora, CO 80045, USA.

10 ²Linda Crnic Institute for Down Syndrome, University of Colorado-Anschutz Medical Campus,
11 Aurora, CO 80045, USA.

12 ³Molecular, Cellular, and Developmental Biology, University of Colorado at Boulder, Boulder,
13 CO 80302, USA.

14 ⁴The Jackson Laboratory, Bar Harbor, ME 04609, USA.

15 ⁵Department of Pharmacology, University of Colorado-Anschutz Medical Campus, Aurora, CO
16 80045, USA.

17 ⁶Department of Pediatrics, Section of Developmental Biology, University of Colorado-Anschutz
18 Medical Campus, Aurora, CO 80045, USA.

19

20 *Correspondence: rytis.prekeris@cuanschutz.edu and chad.pearson@cuanschutz.edu

21 **Abbreviations:** HSA21, human chromosome 21; MMU, mouse chromosome; PCNT,
22 pericentrin; DS, Down syndrome; Shh, Sonic hedgehog; MEF, mouse embryonic fibroblast;
23 RPE1, retinal pigmented epithelia

24

25 **Keywords:** Pericentrin, primary cilia, Trisomy 21, Down syndrome, MyosinVA, CP110, Sonic
26 hedgehog, cerebellar neuronal precursor

27 **Summary**

28 Primary cilia are signaling organelles essential for development and homeostasis. Loss of
29 primary cilia is lethal, and decreased or defective cilia cause multisystemic conditions called
30 ciliopathies. Down syndrome shares clinical overlap with ciliopathies. We previously showed
31 that trisomy 21 diminishes primary cilia formation and function due to elevated Pericentrin, a
32 centrosome protein encoded on chromosome 21. Pericentrin is mislocalized, creating
33 aggregates that disrupt pericentrosomal trafficking and microtubule organization. Here, we
34 examine the cilia-related molecules and pathways disrupted in trisomy 21 and their *in vivo*
35 phenotypic relevance. Utilizing ciliogenesis time course experiments, we reveal how Pericentrin,
36 microtubule networks, and components of ciliary vesicles are reorganized for ciliogenesis in
37 euploid cells. Early in ciliogenesis, chromosome 21 polyploidy results in elevated Pericentrin
38 and microtubule networks away from the centrosome that ensnare MyosinVA and EHD1,
39 blocking mother centriole uncapping that is essential for ciliogenesis. Ciliated trisomy 21 cells
40 have persistent trafficking defects that reduce transition zone protein localization, which is
41 critical for Sonic hedgehog signaling. Sonic hedgehog signaling is decreased and anticorrelates
42 with Pericentrin levels in trisomy 21 primary mouse embryonic fibroblasts. Finally, we observe
43 decreased ciliation *in vivo*. A mouse model of Down syndrome with elevated Pericentrin has
44 fewer primary cilia in cerebellar granule neuron progenitors and thinner external granular layers.
45 Our work reveals that elevated Pericentrin in trisomy 21 disrupts multiple early steps of
46 ciliogenesis and creates persistent trafficking defects in ciliated cells. This pericentrosomal
47 crowding results in signaling defects consistent with the neurological deficits found in individuals
48 with Down syndrome.

49

50 Introduction

51 Trisomy 21 or Down syndrome (DS) is a common chromosomal disorder characterized by
52 phenotypes including craniofacial abnormalities, intellectual disability, heart defects, and
53 cerebellar hypoplasia.¹⁻³ These pathologies overlap with those of ciliopathies—genetic disorders
54 affecting primary cilia.⁴ Primary cilia are concentrated signaling hubs, particularly for the Sonic
55 hedgehog pathway (Shh), and are essential for vertebrate development. The primary cilium
56 nucleates from the centrosome and projects into the extracellular space. The centrosome is
57 comprised of a mother and daughter centriole and surrounding pericentriolar material. Cilia
58 formation requires the spatial and temporal coordination of many molecules. It begins with
59 remodeling the mother centriole, including addition of appendages that serve as docking
60 platforms for cargo delivery.⁵⁻⁷ This triggers removal and proteasomal degradation of the mother
61 centriole capping proteins, allowing extension of axoneme microtubules and membrane
62 remodeling to ensheath the axoneme with a ciliary membrane.^{5,8,9} A barrier complex forms at
63 the base of the cilium called the transition zone, that restricts access to and from the cilium. This
64 creates a unique ciliary compartment that is biochemically distinct from the rest of the cell,
65 allowing the cilium to function as a specialized signaling organelle.¹⁰

66 Building and maintaining signaling cilia requires trafficking of molecules to and from the
67 centrosome.^{11,12} Molecules are trafficked in both membrane-derived vesicles and granular
68 moieties, called centriolar satellites, that move along microtubules nucleated and organized by
69 the centrosome.¹³⁻¹⁵ Pericentrin (PCNT) is an essential centrosome scaffolding protein that,
70 together with CDK5RAP2/CEP215, organizes γ -tubulin and microtubules,^{16,17} and in *Drosophila*
71 the PCNT ortholog is required for cilia function in sensory cells and sperm.¹⁸ *PCNT* is encoded
72 on human chromosome 21 (HSA21), and we previously showed that elevated PCNT due to
73 increased copy number in trisomy 21 is necessary and sufficient to initiate cilia defects in human
74 DS-derived fibroblasts compared to age- and sex-matched controls.¹⁹ Elevated PCNT forms
75 aggregates that colocalize with satellite proteins such as PCM1 and disrupts the flux of

76 intracellular components to and from the centrosome, analogous to a traffic jam.²⁰ While we
77 showed reduced centrosome localization of the ciliary IFT20 protein in trisomy 21 cells,¹⁹ IFT20
78 recruitment to the cilium is a later step in the process of ciliogenesis^{9,21}. Thus, it is unknown
79 which molecules or pathways are disrupted in trisomy 21 that reduce cilia formation and
80 signaling, and whether these cilia defects observed in cultured cells contribute to DS-associated
81 phenotypes *in vivo*.

82 Here, we use isogenic human cell lines to eliminate genetic variability and mouse
83 models of DS to show that elevated PCNT induces trafficking defects around the centrosome
84 such that cargo trafficking events required for early steps in primary ciliogenesis, including
85 ciliary vesicle formation and mother centriole uncapping are held up in a 'pericentrosomal
86 crowd'. Of the trisomy 21 cells that do ciliate, intracellular trafficking defects persist as transition
87 zone proteins are unable to reach the centrosome efficiently, thereby decreasing their
88 localization at the transition zone. Consistent with transition zone defects, Shh signaling is
89 reduced and anticorrelates with PCNT levels. A mouse model of DS with increased *Pcnt* copy
90 number and elevated PCNT levels has reduced primary cilia in both primary mouse embryonic
91 fibroblasts (MEFs) as well as cerebellar neuronal precursor cells *in vivo*. Consistent with ciliary
92 assembly and signaling defects, these mice have a thinner external granular layer and fewer
93 neuronal protrusions. Our findings reveal how early events in ciliogenesis are disrupted by a
94 PCNT-overexpression-induced crowding phenotype and that these ciliation and signaling
95 defects have consequences for *in vivo* brain development in DS.

96

97 **Results (3500 words)**

98 *Rapid PCNT and microtubule reorganization in response to ciliation cues increases with HSA21*
99 *dosage*

100 We previously showed that elevated PCNT is necessary and sufficient for decreased ciliation in
101 trisomy 21 cells.^{19,20} Whereas PCNT normally nucleates and organizes microtubules emanating
102 from centrosomes, elevated PCNT has three major consequences in trisomy 21 cells (Figure
103 1A): 1) PCNT nucleates excess microtubules, thereby increasing microtubule density around
104 the centrosome; 2) PCNT forms large protein aggregates along these microtubules; and 3)
105 PCNT nucleates cytoplasmic microtubules that are disconnected from the centrosome.^{19,20}
106 Together, elevated PCNT perturbs trafficking to and from centrosomes by altering microtubule
107 networks and molecular composition of the pericentrosomal region, thereby hindering the
108 exchange of molecules required for ciliogenesis – pericentrosomal crowding. This model was
109 derived from an analysis of either cycling cells or cells 24 hours after serum depletion (0.5%
110 serum in DMEM) to induce G1 cell cycle arrest and ciliogenesis.^{19,20} We questioned whether
111 elevated PCNT results in an immediate trafficking delay upon induction of ciliogenesis or if
112 trafficking defects build up over time such that only later steps of ciliogenesis are affected.

113 To differentiate between these alternatives, we used human Retinal Pigmented Epithelial
114 (RPE1) cells to perform a time course during ciliogenesis and analyzed how PCNT and
115 microtubule organization change at the centrosome. In RPE1 cells with two copies of HSA21
116 (D21), PCNT levels increased rapidly by approximately 50% near the centrosome (within a 5 μ m
117 radius) 2 hours after serum depletion, and continued to gradually increase throughout the
118 remaining 48-hour time course (Figures 1B, 1C). Similarly, microtubule density around the
119 centrosome fluctuated between 0 and 8 hours post serum depletion, then remained constant
120 through the rest of the time course (Figures 1B, 1D). Isogenic human RPE1 cells genetically
121 engineered to have three or four copies of HSA21 (Trisomy 21/T21 or Tetrasomy 21/Q21), have
122 elevated PCNT prior to serum depletion both at and around the centrosome (within a 5 μ m

123 radius) (Figures 1B, 1C). Microtubule intensity was more similar in all three cell lines prior to
124 serum depletion (Figures 1B, 1D). By 2 hours, both PCNT and microtubule intensities elevated
125 with increasing HSA21 dosage (Figures 1B-D). Elevated PCNT near the centrosome in T21 and
126 Q21 cells persisted through the time course and was not due to changes in whole cell protein
127 levels (Figures 1B-D, S1A-C). Instead, PCNT and microtubules in T21 and Q21 cells
128 reorganized at the centrosome (0.0-1.2 μm region from the centroid of the centrosome) and
129 pericentrosomal region (1.2-5.0 μm region from the centroid of the centrosome), such that more
130 PCNT foci and microtubules were distributed around the centrosome (Figures 1B-D, S1D-G).
131 These data support a model whereby PCNT accumulates at and around the centrosome upon
132 induction of ciliogenesis. Interestingly, by 48 hours, PCNT and microtubule intensities were least
133 changed between the three cell populations (Figures 1B-D, S1D-G), suggesting that T21 and
134 Q21 cells might adapt to an elevated PCNT state upon prolonged G1 arrest.

135 To understand the interplay between PCNT levels, microtubules, and ciliation, we
136 quantified primary cilia frequency through the time course. D21 cells demonstrated two rates of
137 ciliation: a fast phase from 0-8 hours and a slow phase from 8-48 hours (Figures 1E, 1F). In
138 contrast, T21 and Q21 cells showed a decreased initial fast phase; however, the slow phase
139 from 8-48 hours was similar to D21 cells (Figures 1E, 1F). The fast ciliation phase correlates
140 with the early increases to PCNT and microtubule intensities which are more robust in T21 and
141 Q21 cells (Figures 1B-F). The delay in ciliogenesis observed in T21 and Q21 cells is consistent
142 with a model whereby increasing HSA21 dosage disrupts pericentrosomal trafficking flux to and
143 from the centrosome early in the process of ciliogenesis.

144

145 *HSA21 ploidy does not affect centriole appendages but decreases vesicles at the mother*
146 *centriole*

147 Primary ciliogenesis requires coordination between a series of trafficking and complex assembly
148 events over several hours.²² Centriole appendage assembly at the distal end of the mother
149 centriole is an initiating event in ciliogenesis. These appendages serve as a scaffold for
150 receiving ciliary components trafficked to the centrosome.⁵⁻⁷ CEP164 and CEP83 are two distal
151 appendage proteins, with CEP83 adjacent to the centriole microtubule walls and CEP164 at the
152 tip of the appendage structure.²³ In all cell lines (D21, T21, and Q21), CEP164 and CEP83
153 localized normally at the mother centriole (Figures 2A, S2A). Moreover, the subdistal
154 appendage proteins ODF2^{24,25} and Ninein²⁶ correctly localized to the mother centriole (Figures
155 2B, S2B). Thus, HSA21 ploidy does not affect mother centriole appendages.

156 To gain further insight into the ultrastructure of centrioles with increasing HSA21 dosage,
157 we performed 3D electron tomography. Consistent with the immunofluorescence data, D21,
158 T21, and Q21 cells showed ninefold symmetry of distal and subdistal appendages. Moreover,
159 the triplet microtubules that comprise the centriole wall were unchanged across all cell lines,
160 further confirming that HSA21 ploidy does not affect centriole structure. However, 3D modeling
161 of the tomograms revealed changes in the number of vesicles at the mother centriole. D21 cells
162 showed many small vesicles (35-65 nm diameter) near the mother centriole (91 vesicles),
163 whereas vesicle number was decreased in T21 and Q21 cells (26 and 31 vesicles, respectively)
164 (Figure 2D, red spheres). Moreover, in D21 cells, vesicles were distributed along microtubules
165 and at their ends while vesicles in the T21 and Q21 cells were not always found on microtubules
166 (Figure 2D, Video S1-3). Despite the increased microtubule density observed in Figure 1, the
167 comparable number of microtubule minus ends near the centrioles (86, 69, 90 microtubule ends
168 in D21, T21, Q21, respectively) suggests that the additional microtubules are not arising from
169 the mother centriole. Because the tomograms only capture the centrosomal region (0-1.2 μ m
170 from centroid of centrosome), this is consistent with our studies showing that more microtubules
171 are found in the pericentrosomal region that is distal to the centrioles (Figure 1D).²⁰ Together,

172 these data suggest that HSA21 dosage does not affect centriole structure nor centriole
173 appendage formation but may alter membrane structures at and around the centrosome.
174
175 *Preciliary vesicle components contribute to PCNT-induced pericentrosomal crowding*
176 Centriolar appendages are docking sites for delivery of vesicles and molecules required for
177 ciliogenesis.⁵ Our EM tomograms suggested that vesicle accumulation at the mother centriole is
178 defective with HSA21 ploidy. Because increased HSA21 ploidy resulted in changes to the
179 pericentrosomal region in early ciliogenesis, one potential explanation for decreased mother
180 centriole vesicles is disrupted trafficking in the pericentrosomal region. We thus examined
181 whether molecules required for initiating ciliogenesis are disrupted in this region. The first
182 molecules that initiate the downstream steps of ciliogenesis are termed the preciliary or distal
183 appendage vesicle and include the motor protein Myosin VA (MYOVA)⁸ and the membrane
184 shaping protein EHD1.⁹ At 2 hours post serum depletion, about half of D21 cells have formed a
185 MYOVA vesicle at the mother centriole (Figure 3A). In contrast, T21 and Q21 cells show
186 decreased MYOVA vesicle formation and a striking buildup of MYOVA protein in the
187 pericentrosomal region surrounding the centrosome (Figures 3A-B). These changes in
188 pericentrosomal MYOVA intensity were not due to changes in whole cell MYOVA protein levels
189 (Figure S3A). Radial analysis of MYOVA intensity surrounding the centrosome in D21 cells
190 showed high MYOVA levels at the centrosome that then decreased in intensity moving away
191 from the centrosome (Figure 3B inset). We then compared MYOVA intensity distribution at and
192 around the centrosome with increasing ploidy through the time course. Two hours after serum
193 depletion, MYOVA intensities in T21 and Q21 cells were increased in the pericentrosomal 1.2-
194 5.0 μm region from the centroid of the centrosome (Figure 3B). Moreover, centrosomal MYOVA
195 levels were decreased with increasing ploidy (Figure S3B). By 4 hours, pericentrosomal
196 MYOVA intensities in T21 and Q21 cells became more prominent, while MYOVA centrosomal
197 levels remained decreased (Figures 3A, 3C, S3C). By 24 hours, T21 and Q21 cells still showed

198 changes in MYOVA intensity distribution, but the increased intensities were tighter around the
199 centrosome (Figures 3A, 3D, S3D), consistent with the redistribution of PCNT intensities
200 observed between 4 and 24 hours (Figure 1C). Whereas MYOVA intensities increased at the
201 centrosome in T21 and Q21 cells 24 hours post serum depletion, MYOVA appeared more
202 diffuse at the mother centriole compared to D21 cells (Figure 3A, bottom panel). This suggests
203 an additional defect in vesicle coalescence. Taken together, MYOVA intensity increases in the
204 pericentrosomal region with increasing ploidy, and we define this pericentrin-induced
205 redistribution of molecules around the centrosome with increasing HSA21 ploidy as
206 pericentrosomal crowding.

207 We then asked whether elevated PCNT found with increased HSA21 ploidy was
208 sufficient to increase MYOVA in the pericentrosomal crowding region. We have previously
209 shown that reducing PCNT levels in T21 and Q21 cells with siRNA rescues ciliation.²⁰ Reducing
210 PCNT levels in T21 and Q21 cells to D21 levels with siRNA at 24 hours post serum depletion
211 rescued the increased centrosomal and pericentrosomal MYOVA intensity to D21 levels
212 (Figures 3E, 3F, S3E, S3F). Moreover, the pericentrosomal increase in MYOVA consistently
213 increases with increasing PCNT levels (Figures S3G, S3H). Thus, elevated PCNT from
214 increasing HSA21 ploidy induces pericentrosomal crowding where MYOVA accumulates during
215 early ciliogenesis, thereby preventing efficient MYOVA vesicle formation at the mother centriole.

216 We next examined EHD1, an early vesicle protein that is recruited to the mother
217 centriole for coalescence and fusion of preciliary or distal appendage vesicles.⁹ We observed
218 decreased EHD1 accumulation at the mother centriole with increasing ploidy and a slight
219 increase in EHD1 that is caught up in the pericentrosomal region (Figure S3I). Together, our
220 data support a model whereby elevated PCNT in trisomy 21 accumulates at and around the
221 centrosome immediately after induction of ciliogenesis and induces pericentrosomal crowding,
222 disrupting multiple trafficking pathways required for early preciliary vesicle formation.

223

224 *Increased HSA21 ploidy disrupts mother centriole uncapping in a PCNT-dosage dependent*
225 *manner*

226 Delivery of preciliary vesicles occurs just prior to or coincident with mother centriole uncapping,⁸
227 which involves removal and degradation of the centriole capping proteins CP110 and
228 CEP97.^{27,28} Both CP110 and CEP97 removal from mother centrioles is defective in T21 and
229 Q21 cells compared to D21 cells (Figures 4A, S4A-C). To determine if these uncapping defects
230 were due to elevated PCNT levels, we decreased PCNT levels in T21 and Q21 cells back to
231 D21 levels and examined uncapping. Strikingly, reduced PCNT levels rescued CP110 removal
232 from the mother centriole (Figure 4B). Together, this indicates that elevated PCNT from
233 increased HSA21 ploidy is sufficient to block mother centriole uncapping. Because uncapping
234 requires the trafficking of the preciliary vesicle, we propose that elevated PCNT-induced
235 crowding ensnares components required for efficient uncapping (Figure 4E).

236 The small GTPase RAB8 functions in ciliary membrane extension during later steps in
237 ciliogenesis.⁹ We previously showed that IFT20 is reduced at the centrosome in patient-derived
238 trisomy 21 fibroblasts.¹⁹ IFT20 is recruited to the mother centriole upstream of RAB8 and is
239 required for RAB8 targeting to the ciliary membrane.^{9,21} We thus examined RAB8 localization to
240 the mother centriole during the ciliogenesis time course to determine if later trafficking pathways
241 are also disrupted. By 8 hours post serum starvation, T21 and Q21 cells showed decreased
242 RAB8 accumulation at the mother centriole compared to D21, and this decrease persisted
243 throughout the time course (Figures 4C-D, S4D). Given that RAB8 associates with Golgi and
244 post-Golgi membranes in the context of ciliogenesis,^{29,30} one potential explanation for
245 decreased RAB8 at the centrosome is defective trafficking from the Golgi. However, we did not
246 observe changes in RAB8 intensity at the Golgi with increasing ploidy, suggesting RAB8 leaves
247 the Golgi without incident (Figures S4E-F). Thus, RAB8 trafficking defects are specific to the
248 centrosomal region and are not generally disrupted intracellularly in T21 and Q21 cells.

249 Given the observed defects in trafficked proteins required for ciliogenesis reaching the
250 centrosome and the importance of microtubules in trafficking pathways, we wondered if general
251 membrane trafficking pathways were disrupted with increasing HSA21 ploidy. *Cis*- and *trans*-
252 Golgi networks, early endosomes, and lysosomes did not exhibit changes in morphology in T21
253 and Q21 cells when compared to D21 cells (Figures S4G-Q). Moreover, whereas mild intensity
254 differences were observed in some of these organelles, they did not follow a consistent trend
255 with increasing ploidy (Figures S4G-Q). Thus, gross disruptions of the endolysosomal trafficking
256 pathways are not apparent and trafficking defects associated with trisomy 21 are focused at and
257 around the centrosome with increasing HSA21 ploidy. Collectively, this suggests that
258 ciliogenesis defects in trisomy 21 result from early PCNT-induced crowding around the
259 centrosome that captures preciliary vesicle components thereby preventing mother centriole
260 uncapping and RAB8-axoneme extension.

261

262 *Decreased transition zone protein localization in ciliated trisomy 21 cells*

263 Despite early defects in ciliogenesis, elevated PCNT from increasing HSA21 ploidy does not
264 abolish cilia. Approximately 40% of T21 and 20% of Q21 cells formed a primary cilium by 24
265 hours post serum depletion (Figure 1E). We thus wondered whether trisomy 21 induced a
266 purely kinetic block in cilia formation or if defects persisted after ciliation. To function as a
267 signaling compartment, primary cilia are exposed to the external cellular environment to send
268 and receive signals. In RPE1 cells, cilia assemble inside the cell and then fuse with the cell
269 membrane to become extracellular signaling organelles.³¹ This requires remodeling of the
270 plasma membrane and cytoskeletal networks. Given the observed centrosomal trafficking
271 defects, we tested whether cilia in trisomy 21 cells were exposed to the external environment
272 using the IN/OUT assay.³² No difference was observed in the number of cilia outside versus
273 inside the cell in D21 and T21 cells (Figure S5A-B), suggesting that trisomy 21 does not cause
274 cilia to be retained inside cells.

275 A second requirement for cilia function in signaling is the creation of a diffusion barrier
276 called the transition zone. The transition zone, at the base of the cilium, is composed of proteins
277 that regulate entry and exit of molecules to and from the cilium. Regulation of diffusion through
278 the transition zone is essential for proper ciliary signaling, and many genes mutated in
279 ciliopathies encode transition zone proteins.^{33,34} The levels of transition zone proteins were
280 analyzed in D21 and T21 cells. Q21 cells were eliminated because of their low ciliation
281 frequency. Consistent with defects in the primary cilia transition zone, the core transition zone
282 protein CEP290^{35,36} was decreased in T21 cells compared to D21 cells (Figures 5A, yellow
283 arrows, and 5B). In addition to the transition zone, CEP290 also localizes to centriolar
284 satellites¹³, and we observed increased CEP290 at the pericentrosomal but not centrosomal
285 region in T21 cells relative to D21s (Figures 5A, 5C, S5C). Moreover, CEP290 colocalizes with
286 PCNT in this pericentrosomal region (Figure 5A, cyan arrows), suggesting that decreased
287 CEP290 at the transition zone may result from pericentrosomal crowding. In addition to
288 CEP290, RPGRIP1L, and two outer transition zone proteins, NPHP4 and TMEM67,³⁷ were also
289 decreased at the transition zone in T21 compared to D21 cells (Figures 5D-I). Collectively,
290 trisomy 21 cells show transition zone defects suggesting that trafficking problems to the
291 centrosome are not specific to building a cilium but persist even in ciliated cells. This may
292 explain the signaling defects found previously in cells with elevated PCNT.¹⁹

293

294 *Shh signaling is defective in primary mouse fibroblasts with elevated PCNT*

295 The barrier function of the transition zone is critical for proper ciliary signaling.^{34,38} Because
296 transition zone defects were found in trisomy 21 cells, we next asked whether trisomy 21
297 negatively affects primary cilia dependent signaling. Shh signaling is the best understood cilia-
298 dependent signaling pathway and is important for developmental events that are impacted in
299 DS. Moreover, Shh signaling was previously found to be disrupted in a DS mouse model.³⁹ Shh
300 signaling is commonly studied in primary mouse embryonic fibroblasts (MEFs). HSA21 maps to

301 syntenic regions of three mouse chromosomes: MMU10, MMU16, and MMU17.⁴⁰ We analyzed
302 three mouse models harboring segmental genomic duplications of these syntenic regions on
303 MMU10, MMU16, or MMU17 called Dp10, Dp16, or Dp17, respectively.⁴¹ The murine *Pcnt* gene
304 is located on MMU10, therefore only the Dp10 model contains an extra copy of the *Pcnt* gene,
305 although other cilia and centrosome-related genes can be found on MMU16 and MMU17
306 (Figure 6A).^{19,42}

307 We first asked whether MEFs isolated from Dp10, Dp16, or Dp17 embryos showed
308 ciliation defects. Strikingly, only the Dp10 MEFs with elevated PCNT showed decreased primary
309 cilia frequency when compared to wild-type littermates (Figures 6B-E). Cilia frequency in Dp16
310 and Dp17 MEFs was identical to wild-type (Figures 6C, S6A-B). Dp10 mice contain
311 approximately 41 duplicated HSA21 gene orthologs,⁴¹ and we previously tested the other cilia
312 and centrosome human orthologs on MMU10 and found no changes in ciliation.¹⁹ Thus,
313 decreased ciliation is specific to elevated PCNT in primary MEFs from the Dp10 mouse model
314 of DS.

315 Upon induction of the Shh pathway, the transmembrane protein Smoothed (SMO)
316 translocates into the cilium and generates signals that induce nuclear GLI localization and
317 downstream transcriptional response of hedgehog target genes important for mitogenic activity
318 and developmental processes such as patterning and limb development.^{4,43} Because Shh
319 signaling is disrupted in a DS mouse model,³⁹ and we previously found decreased GLI
320 expression in DS-derived human fibroblasts,¹⁹ we next examined Shh signaling in MEFs where
321 we can distinguish the contributions of different regions of HSA21. We compared SMO intensity
322 in the cilium with and without induction of Shh signaling using the SMO agonist SAG. Without
323 SAG, ciliary SMO levels were undetectable in both wild-type and Dp10 MEFs (Figures 6F and
324 6H). However, upon SAG treatment, SMO robustly accumulated in the cilium in wild-type cells,
325 whereas ciliary SMO remained low in Dp10 cells (Figures 6G-H). Moreover, ciliary SMO levels
326 in Dp16 and Dp17 cell lines after SAG treatment were the opposite of PCNT levels, as Dp16

327 MEFs had slightly elevated PCNT levels and slightly decreased ciliary SMO while Dp17 MEFs
328 had slightly decreased PCNT levels and slightly increased ciliary SMO (Figures 6D-E, 6H, S6C-
329 D). Together, decreased ciliation frequency and ciliary SMO in Dp10 MEFs is consistent with
330 persistent trafficking defects from pericentrosomal crowding in ciliated trisomy 21 cells.
331 Moreover, PCNT levels anticorrelate with ciliary SMO in Dp16 and Dp17 MEFs.

332 Interestingly, one Dp10 MEF line (Dp10-2) did not show decreased ciliation compared to
333 wild-type controls (Figures S6E-F). Importantly, this line also did not exhibit elevated PCNT
334 levels or defects in ciliary SMO localization upon SAG treatment (Figures S6G-H). It is unclear
335 whether this Dp10-2 line lost the chromosome duplication containing PCNT or whether cells
336 compensated at the molecular level. Regardless, results from this line reinforce the conclusion
337 that cilia and signaling defects result from elevated PCNT levels. In summary, PCNT and ciliary
338 SMO levels anticorrelate and are disrupted in trisomy 21.

339

340 *Elevated PCNT in a DS mouse model results in decreased primary cilia and cerebellar* 341 *dysmorphology*

342 Primary cilia are ubiquitous and essential signaling organelles. They are particularly important
343 during brain development and are predicted to be disrupted in DS.^{4,44} Individuals with DS
344 commonly exhibit cerebellar hypoplasia,¹ and delayed cerebellar development has been
345 observed in the Ts65Dn mouse model of DS, which harbors a duplication of MMU16 genes
346 similar to that of the Dp16 model along with a duplication of genes from MMU17 that are not
347 syntenic to human HSA21.^{39,40} During cerebellar development, neuronal precursor cells in the
348 external granular layer respond to Shh from Purkinje cells.^{45,46} Shh induces mitogenic activity,
349 and the amplified cells ultimately migrate to the internal granule layer where they become
350 mature neurons.⁴⁶ Primary cilia are required for neuronal precursor cell amplification and
351 defects in Shh signaling reduce proliferation and disrupt cerebellar development.⁴⁷ Yet, whether
352 T21 and elevated PCNT disrupt primary cilia during brain development *in vivo* remains

353 unknown. We therefore examined ciliation in the external granular layer of postnatal day 4 (P4)
354 pups. Consistent with our findings in Dp10 MEFs, cerebellar neuronal precursors in Dp10
355 animals had fewer primary cilia compared to wild-type littermates (Figures 7A, 7D). Moreover,
356 Dp16 and Dp17 animals showed no change in ciliation frequency (Figures 7B-D). These data
357 are consistent with our analyses in MEFs suggesting that cilia defects occur in animals with
358 elevated PCNT.

359 Reduced Shh signaling correlates with morphological changes in the cerebellum, such
360 as decreased width of the external granular layer.^{48,49} We thus measured the width of the
361 external granular layer and found decreased widths in Dp10 animals compared to wild-type
362 littermates (Figure 7E-F). Decreased width could result from decreased cell proliferation, so we
363 next examined Ki67 staining as a marker for cell proliferation. While we observed no changes in
364 the number of Ki67-positive cells in the external granular layer of Dp10 and wild-type animals at
365 P4 (Figure S7A-B), we cannot rule out changes in cell proliferation at earlier developmental time
366 points. The source of Shh for neuronal precursors comes from Purkinje cells,⁴⁶ so we next
367 examined the Purkinje cell layer. No loss of Purkinje cells was noted between Dp10 and wild-
368 type siblings (Figure S7C). Finally, given that elevated PCNT alters microtubule networks in
369 cultured RPE1 cells and that PCNT mutations produce severe neuronal defects including
370 disrupted neuronal migration,^{18,50,51} we visualized doublecortin (DCX), a microtubule binding
371 protein that functions in neuronal migration.^{52,53} Interestingly, Dp10 animals showed decreased
372 DCX-labeled cellular protrusions compared to wild-type (Figure S7C). While not conclusive, this
373 suggests that elevated PCNT alters non-centrosomal microtubules such as those required for
374 neuronal outgrowth.⁵⁴ Taken together, elevated PCNT results in decreased ciliation in the
375 external granular layer of the cerebellum and these cerebella demonstrated morphology
376 changes consistent with decreased Shh signaling and developmental defects.

377 To determine if decreased ciliation *in vivo* was a direct result of elevated PCNT levels,
378 we cultured cerebellar slices from P4 pups and treated slices with either control or PCNT

379 siRNA. Strikingly, reducing PCNT levels in Dp10 slice cultures rescued ciliation back to control
380 levels (Figure 7G-I). Taken together, this suggests that elevated PCNT from trisomy 21 is
381 sufficient to induce ciliation defects during cerebellar development *in vivo*.

382 Our data from T21 and Q21 RPE1 cells suggested that pericentrosomal crowding
383 delayed ciliogenesis; however, cells arrested in G1 for a prolonged period eventually ciliated
384 albeit at slightly lower frequencies than D21 cells (Figure 1E). Moreover, our previous work in
385 human DS-derived fibroblasts showed the strongest ciliation defects in cycling cells.¹⁹ We thus
386 tested whether ciliation defects *in vivo* were dependent on cell cycle state by analyzing cells in
387 the inner granular layer of the cerebellum which are generally post-mitotic. Primary ciliation of
388 inner granule layer cells was unchanged between wild-type and Dp10 animals (Figure S7D).
389 This provides further evidence that trisomy 21 alters but does not abolish ciliogenesis *in vivo*,
390 with the major impact on migrating precursor cells

391

392 Discussion

393 *Trisomy 21 alters trafficking flux of early ciliogenesis molecules delaying ciliogenesis*

394 Here, we use a time course to establish the dynamic changes to PCNT trafficking puncta and
395 microtubules upon induction of ciliogenesis through media serum depletion. In control euploid
396 cells, the largest changes to PCNT and microtubule networks around the centrosome occur
397 early, within 2 h after induction of ciliogenesis. Moreover, we observe a slow and a fast phase to
398 ciliation in a population of cells, with the fast phase occurring within the first 8 h and the slow
399 phase from 8-48 h. In T21 and Q21 cells, PCNT and microtubule levels increase more
400 dramatically at the onset of ciliogenesis. This is accompanied by a decrease in the effectiveness
401 of the fast phase of ciliogenesis, while the slow phase from 8 to 48 h is largely the same as D21
402 cells. These data reveal that in trisomy 21, PCNT-induced pericentrosomal crowding occurs
403 immediately upon induction of ciliogenesis and delays but does not abolish ciliation.

404 Several distinct trafficking pathways required for building a primary cilium are prevented
405 from efficient recruitment to the site of assembly in the altered microtubule and PCNT landscape
406 caused by increased HSA21 dosage. MYOVA, one of the earliest proteins to localize to the
407 mother centriole, does not traffic normally but rather participates in pericentrosomal crowding in
408 T21 and Q21 cells. Mother centriole uncapping is also disrupted, perhaps through defects in
409 trafficking the ubiquitin or autophagosome machinery required for CP110 and CEP97 removal
410 and degradation, although this remains to be tested. In addition to early defects in ciliogenesis,
411 pericentrosomal crowding affects later steps such as RAB8-mediated ciliary membrane growth
412 and IFT20 centrosomal localization.^{9,19} Together, our results show HSA21 dosage dependent
413 disruption in trafficking pathways important to the earliest observable stages of ciliogenesis and
414 cilia function, as molecules required for building and maintaining a cilium get hung up in PCNT-
415 induced crowding around the centrosome.

416 Consistent with a crowding model, several lines of evidence support the idea that
417 trisomy 21 does not result in a complete block to ciliogenesis, but rather a delay in the process.

418 First, with sustained G1 arrest, T21 and Q21 cells increase their ciliation, and these cells appear
419 to compensate for crowding such that the difference between PCNT and microtubule densities
420 at and around the centrosome is reduced between D21, T21, and Q21 cell lines. Second, a
421 similar phenomenon is observed with crowding cargo, as the amount of pericentrosomal
422 MYOVA decreases over time and MYOVA eventually accumulates at mother centrioles in T21
423 and Q21 cells. Third, trisomy 21 cells demonstrate defective signaling even after a cell builds a
424 primary cilium. This is consistent with previous work showing reduced GLI expression in human
425 trisomy 21 cells and decreased ciliary SMO trafficking in cells overexpressing PCNT.¹⁹ Fourth,
426 crowding has the most severe consequences for molecules that are dynamically trafficking to
427 and from the centrosome, whereas longer lived structures such as the core centriole and
428 appendages⁵⁵ are unaffected by elevated PCNT. Finally, *in vivo*, only cycling neuronal
429 precursors of the external granular layer have decreased ciliation, whereas ciliation in post-
430 mitotic cells of the inner granular layer remains unaffected with trisomy 21. Collectively, we find
431 that PCNT-induced pericentrosomal crowding disrupts the dynamic flux of molecules to and
432 from the centrosome thereby disturbing the coordination and timing required for proper
433 ciliogenesis and signaling.

434

435 *Cerebellar phenotypes in animals with elevated PCNT*

436 While the timing of ciliogenesis is not vital in cultured cells, the timing of ciliogenesis and cilia-
437 dependent signaling is critical during *in vivo* development where cilia send and receive input
438 from neighboring cells to coordinate proper tissue development.⁴⁴ In line with our cultured cell
439 results, we do not observe a complete loss in cilia and signaling in primary MEFs or cerebellar
440 neuronal precursor cells with elevated PCNT but do observe consistent decreases in ciliation.
441 Moreover, the organization of cerebellar layers with a thinner external granular layer is altered
442 but not eliminated. While we might expect to see decreased cell proliferation in cells in the
443 external granular layer, Ki67 staining, a marker for proliferating cells, appears normal in Dp10

444 animals compared to wild-type littermates. This result could occur for several reasons. First, our
445 analysis was conducted only in P4 pups, where developmental delays are not yet obvious in
446 Dp10 animals. An analysis of cell proliferation at earlier or later timepoints might show changes
447 to the number of cycling cells. Second, because elevated PCNT does not result in a complete
448 loss of cilia, perhaps enough of the cell population is ciliated to receive the Shh mitogenic signal
449 and proliferate at this timepoint. Cerebellar development is a highly integrated process where a
450 trisomy 21-induced delay in ciliogenesis could alter the coordination of cellular processes such
451 that some cells never fully catch up. Because inputs are not completely lost, this cell-to-cell
452 variability could account for the spectrum of phenotypes observed in individuals with DS.

453 Most trisomy 21 animal studies have been performed in the Ts65Dn mouse model.⁴⁰
454 While these mice show some degree of DS-like phenotypes, they are only trisomic for about half
455 of the HSA21 orthologs and contain an additional amplification of genes not found on
456 HSA21.^{40,56} The Dp mouse models are a more refined genetic system to determine the
457 phenotypic contributions from different regions of HSA21. Dp10 mice contain approximately 41
458 duplicated HSA21 gene orthologs including PCNT while Dp16 and Dp17 mice have 115 and 19
459 duplicated gene orthologs, respectively, and exclude PCNT.⁴¹ Our experiments in primary MEFs
460 and cerebellar slices largely attribute cilia defects to elevated PCNT levels in Dp10 animals.
461 However, there are other known cilia and centrosome genes found on HSA21, and potentially
462 non-coding regions that may also contribute to phenotypic consequences of trisomy 21. For
463 example, MMU16 contains the splicing factor SON, which is known to splice PCNT mRNA and
464 alters PCNT levels and distributions.^{57,58} Indeed, while we do not find changes in primary cilia
465 frequency in Dp16 animals, we do observe moderately decreased ciliary SMO and moderately
466 increased PCNT levels. Interestingly, Dp16 mice have defects in the motile cilia lining the
467 ependymal cells of the brain (Figure S7E-G) suggesting that elevated gene dosage can have
468 different phenotypic consequences in different tissues. In support of this, animals with individual
469 chromosomal duplications, Dp10, Dp16, or Dp17,⁴¹ do not show as severe phenotypic

470 consequences as combined Dp10; Dp16; Dp17 animals.⁵⁹ Therefore, while elevated PCNT
471 disrupts ciliogenesis and signaling, there are likely other contributions from additional genes on
472 HSA21 that add to the spectrum of phenotypes observed in individuals with DS.

473 In contrast to single gene disruption studies, here we show that ciliary defects arise from
474 elevated protein expression, as is often the case in chromosomal aberrations. Indeed, cilia
475 defects have been observed with increased copy number of a nuclear pore protein.⁶⁰ While
476 changes in some protein levels may be tolerated, we demonstrate that even a modest increase
477 in PCNT protein (1.5 - 2-fold) is deleterious to cilia formation and function in a dose dependent
478 manner. Elevated PCNT aggregates and reorganizes microtubule networks, inducing
479 pericentrosomal crowding that disrupts cargo transport required for early steps in ciliogenesis
480 and persists in ciliated trisomy cells. Because tight control of microtubule organization is
481 essential for many cell types and processes including neuron outgrowth, cell migration, immune
482 synapse formation, and cell polarity, these functions need further study to determine whether
483 elevated PCNT from trisomy 21 and changes in microtubule topologies alter these cell types
484 and functions.

485 **Acknowledgements**

486 We thank Drs. Andrew Lane and David Pellman for RPE1 D21, T21, and Q21 cell lines, Dr.
487 Chris Westlake for EHD1 plasmid, Dr. Rajat Rohatgi for SMO antibody, Dr. Tamara Caspary for
488 advice on isolating primary MEFs, and Dr. Derek Toomre for pH-Smoothened plasmid. We are
489 grateful to Drs. Carolyn Ott, Santos Franco, and the Pearson lab for helpful discussions.
490 Electron microscopy was done at the University of Colorado, Boulder EM Services Core Facility
491 in the MCDB Department with Garry Morgan providing specimen preparation. This research
492 was funded by NIH R01GM138415 and R35GM140813 to CGP, NSF Graduate Research
493 Fellowship DGE-1553798, NIH INCLUDE T32 supplement GM008730, and Blumenthal
494 Fellowship to CEJ, and NIH R01DK064380 to RP. CEJ, JME, KDS, and CGP are members of
495 the Linda Crnic Institute for Down syndrome.

496

497 **Author Contributions**

498 CEJ, BLM, ETO, KSG, CHL, and VO performed experiments and analyzed data. CEJ and CGP
499 conceived the project and wrote the manuscript. WM, LR, JME, KDS, WBM, and RP provided
500 reagents, animal models, and expertise.

501

502 **Competing Interests**

503 The authors declare no competing interests.

504

505 **Figure Legends**

506 *Figure 1. Rapid PCNT and microtubule reorganization in response to ciliation cues increases*
507 *with HSA21 dosage.* (A) Model figure showing the three main consequences of elevated PCNT
508 in trisomy 21 (T21) and tetrasomy 21 (Q21) compared to disomy 21 (D21) cells: 1) PCNT
509 nucleates more microtubules; 2) PCNT forms large protein aggregates on microtubules; and 3)
510 PCNT nucleates microtubules further away from the centrosome. These changes occur
511 predominantly in the pericentrosomal region defined as 1.2-5 μm from the centroid of the
512 centrosome. (B) Representative confocal images from time course experiments of RPE1 D21,
513 T21, and Q21 cells grown on coverslips and serum depleted for 0, 2, 4, 8, 24, and 48 h. Cells
514 were stained with DM1a to label microtubules (MTs) and PCNT. Arrows point to cilium labeled
515 by DM1a staining. (C) Quantitation of PCNT intensities in a 5 μm radial circle around the
516 centrosome throughout the time course normalized to D21 average at 0 h. Graph shows mean \pm
517 SD. (D) Quantitation of microtubule intensities in a 5 μm radial circle around the centrosome
518 throughout the time course normalized to D21 average at 0 h. Graph shows mean \pm SD. (E)
519 Quantitation of ciliation frequency throughout the time course using DM1a as a marker for cilia.
520 Graph shows mean \pm SD. N's and statistical tests are listed in Table S1.

521
522 *Figure 2. HSA21 ploidy does not affect centriole appendages but decreases vesicles at the*
523 *mother centriole.* (A-B) Representative SIM images of RPE1 D21, T21, and Q21 cells grown on
524 coverslips and serum depleted for 24 h. Cells were stained with GT335 and the distal
525 appendage marker CEP164 (A) or the subdistal appendage marker ODF2 (B). Percentages
526 represent cells with indicated marker for 3 N's. (C) EM tomograms of RPE1 D21, T21, and
527 Q21 cells serum depleted for 24h showing microtubule triplets and distal appendages (top panel)
528 and subdistal appendages (bottom panel). (D) 3D models of EM tomograms at centrosome. Top
529 row shows mother centriole (yellow), daughter centriole (magenta), microtubule minus ends
530 (light blue spheres), and vesicles (red). Bottom row shows models with microtubules (green)

531 and vesicles displayed. Tomograms and models shown are of cells prior to ciliary vesicle
532 formation.

533

534 *Figure 3. Preciliary vesicle components contribute to PCNT-induced pericentrosomal crowding.*

535 (A) Representative structured illumination microscopy (SIM) images from time course
536 experiments of RPE1 D21, T21, and Q21 cells grown on coverslips and serum depleted for 2, 4,
537 and 24 h. Cells were stained with GT335 to label centrioles and MYOVA. (B-D) Distribution of
538 MYOVA intensities moving away from the centrosome for 2 (B), 4 (C), and 24 (D) h timepoints.
539 (E) Quantitation of centrosomal MYOVA intensity in 0-1.2 μm region around centrosome for
540 control and siPCNT treated D21, T21, and Q21 cells. (F) Quantitation of pericentrosomal
541 MYOVA intensity in 1.2-5 μm region around centrosome for control and siPCNT treated D21,
542 T21, and Q21 cells. All values were normalized to the D21 average, and graphs show mean \pm
543 SD. N's and statistical tests are listed in Table S1.

544

545 *Figure 4. Increased HSA21 ploidy disrupts mother centriole uncapping in a PCNT-dosage*

546 *dependent manner.* (A) Representative SIM images of RPE1 D21, T21, and Q21 cells grown on
547 coverslips and serum depleted for 24 h. Cells were stained with GT335 and the centriole
548 capping protein CP110. Percentages represent cells with indicated phenotype across 3 N's. (B)
549 Quantitation of CP110 centriole capping for control and siPCNT treated D21, T21, and Q21
550 cells. (C) Representative SIM images of RPE1 D21, T21, and Q21 cells grown on coverslips
551 and serum depleted for 4, and 8 h. Cells were stained with γ -tubulin, Actub, and RAB8.
552 Percentages represent cells with indicated phenotype across 3 N's. All time points are shown in
553 Figure S3D. (D) Quantitation of cells with RAB8-positive ciliary vesicle throughout the time
554 course. (E) Cartoon model depicting altered distribution of MYOVA from the mother centriole to
555 the pericentrosomal region and decreased mother centriole uncapping with increasing ploidy.
556 Graphs shows mean \pm SD. N's and statistical tests are listed in Table S1.

557

558 *Figure 5. Decreased transition zone protein localization in ciliated trisomy 21 cells. (A)*

559 Representative confocal images of RPE1 D21 and T21 cells grown on coverslips and serum

560 depleted for 24 h. Cells were stained with GT335, PCNT, and the transition zone protein

561 CEP290. Yellow arrows point to the CEP290 transition zone population and cyan arrows point

562 to CEP290 satellites that colocalize with PCNT. (B) Quantitation of CEP290 transition zone

563 intensity. (C) Quantitation of pericentrosomal CEP290 intensity in 1.2-5 μm region around

564 centrosome. (D, F, H) Representative SIM images of RPE1 D21 and T21 cells grown on

565 coverslips and serum depleted for 24 h. Cells were stained with GT335 and the transition zone

566 proteins RPGRIP1L (D), NPHP4 (F), or TMEM67 (H). (E, G, I) Quantitation of indicated

567 transition zone protein intensities from confocal images. All values were normalized to the D21

568 average, and graphs show mean \pm SD. Mean intensity values are indicated on graphs. N's and

569 statistical tests are listed in Table S1.

570

571 *Figure 6. Shh signaling is defective in primary mouse fibroblasts with elevated PCNT. (A)*

572 Cartoon model depicting mouse syntenic regions with HSA21 and corresponding Dp10, Dp16,

573 and Dp17 mouse models. PCNT is located on MMU10. Other cilia and centrosome proteins are

574 also listed. For all following experiments, WT and Dp primary MEFs were isolated from E12.5

575 dams, grown on coverslips, and serum depleted for 24 h. (B) Representative confocal images of

576 WT and Dp10 MEFs. Cells were stained with Hoechst, the ciliary marker ARL13B, and Actub.

577 (C) Quantitation of the number of cells with a primary cilium in WT and Dp MEFs. (D)

578 Representative confocal images of WT and Dp10 MEFs. Cells were stained with PCNT and

579 ARL13B. (E) Quantitation of PCNT intensities in a 5 μm radial circle around the centrosome in

580 WT and Dp MEFs. Values were normalized to the WT average. (F, G) Representative confocal

581 images of WT and Dp10 MEFs untreated (F) or treated with 100 nM SAG for the last 4 h of

582 serum depletion (G). Cells were stained with SMO and ARL13B. (H) Quantitation of ciliary SMO

583 levels in SAG-treated cells for WT and Dp MEFs. Graphs show mean \pm SD. N's and statistical
584 tests are listed in Table S1.

585

586 *Figure 7. Elevated PCNT in a DS mouse model results in decreased primary cilia and cerebellar*
587 *dysmorphology.* (A-C) Representative tiled confocal images of the cerebellum from P4 wild-type
588 (WT) and Dp10 (A), Dp16 (B), and Dp17 (C) animals. Brain sections were stained with Hoechst,
589 ARL13B, and γ -tubulin. Insets show progressively zoomed in regions corresponding to the same
590 folia in each animal. (D) Quantitation of primary cilia frequency in WT and Dp animals
591 normalized to WT. (E) Representative tiled confocal images of WT and Dp10 P4 animals
592 corresponding to the same cerebellar folia in each animal. Brain sections were stained with
593 Hoechst and a Pan-neuronal marker. Yellow bracket denotes external granular layer. (F)
594 Quantitation of the external granular layer width in WT and Dp10 animals. (G) Quantitation of
595 primary cilia frequency in WT and Dp10 cerebellar slice cultures treated with control or PCNT
596 siRNA. Values were normalized to WT siControl averages. (H) Representative confocal images
597 of WT and Dp10 cerebellar slice cultures isolated from P4 pups and treated with control or
598 PCNT siRNA for 48 h in serum free media. Slices were stained with Hoechst, ARL13B, PCNT.
599 Yellow box denotes insets. (I) Quantitation of PCNT intensity in WT and Dp10 cerebellar slice
600 cultures treated with control or PCNT siRNA. Values were normalized to WT siControl
601 averages.

602 **Materials and Methods**

603 *Cell lines*

604 Disomy 21, Trisomy 21, and Tetrasomy 21 (D21, T21, Q21) hTERT-immortalized retinal
605 pigment epithelial (RPE1) cells were generated by and Drs. Andrew Lane and David Pellman at
606 the Dana-Farber Cancer Institute.⁶¹ Cells were grown in DMEM:F12 (SH30023; Cytiva)
607 supplemented with 10% fetal bovine serum (FBS, Peak Serum; PS-FB2) and 1%
608 Penicillin/Streptomycin at 37°C and 5% CO₂. Cells were passaged 1:5 at ~80-90% confluency
609 with 0.25% Trypsin (15090-046; Gibco). Cells were routinely screened for mycoplasma. Primary
610 MEFs were generated as described in Mariani et al.⁶² In brief, embryonic day 12.5 embryos
611 were dissected from pregnant females. The head and internal organs were removed, and the
612 remaining tissue was dissociated by passage through a needle. The head was used for
613 genotyping. Dissociated cells were cultured in DMEM:F12 with 10% fetal bovine serum and 1%
614 Penicillin/Streptomycin for no more than 3 passages.

615

616 *Immunofluorescence*

617 Cells were plated on collagen-coated coverslips and grown in full media until 80-90% confluent.
618 To induce ciliogenesis, cells were washed once with 1x PBS and then grown in serum depleted
619 media (DMEM:F12 with 0.5% FBS) for indicated hours. For time course experiments, cells were
620 fixed according to Waterman-Storer and Salmon⁶³ following 0, 2, 4, 8, 24, or 48 hours post
621 serum depletion. Briefly, cells were pre-permeabilized for 5 minutes in 0.5% TritonX-100 in
622 PHEM (60mM Pipes, 25mM HEPES, 10mM EGTA, 2mM MgCl₂, 6.9 pH). Cells were then fixed
623 with 4% paraformaldehyde/0.5% glutaraldehyde for 20 minutes and quenched with 0.1%
624 sodium borohydride. Following quenching, cells were washed four times in 0.1% TritonX-100
625 and stored in PHEM at 4°C until immunostaining.

626 For all other staining experiments, cells were fixed with 4% paraformaldehyde for 20
627 minutes at room temperature or with 100% ice cold Methanol for 10 minutes at -20°C. Cells

628 were blocked for 1-2 hours in block buffer (PBS, 0.1% Triton X-100, 10% normal donkey
629 serum). Primary antibodies were diluted in block buffer and incubated overnight at room
630 temperature. Cells were washed with PBSTx before adding secondary antibodies for 1-2 hours
631 at room temperature. Cells were washed again before mounting in VectaShield and sealing with
632 nail polish or mounting in Prolong Gold for SIM experiments. Coverslips for all experiments were
633 #1.5. Primary and secondary antibodies are listed in the Key Resources Table.

634 For SAG treatment, MEFs were grown on coverslips to 80-90% confluency, moved to
635 serum depleted media for 20 hours, treated with 100 nM SAG in serum depleted media for 4
636 hours, fixed with 4% PFA and stained as described above.

637 To costain PCNT with other rabbit primary antibodies, PCNT was conjugated to Alexa
638 Fluor 488 (Antibody labeling kit: Invitrogen A20181).

639

640 *Fluorescence microscopy*

641 Confocal images were acquired using either a Nikon Eclipse Ti 2 inverted A1 Confocal and
642 Nikon Elements software or Nikon Eclipse Ti inverted microscope stand equipped with a 100x
643 Plan Aplanachromat objective (NA 1.45), Andor iXon X3 camera, CSU-X1 (Yokogawa) spinning
644 disk, and Slidebook 6 software. Super resolution imaging was performed on a Nikon 3D SIM
645 system (Ti 2 Eclipse) with a 100x TIRF objective (NA 1.45). Images were captured with a
646 complementary metal-oxide semiconductor camera (Orca-Flash 4.0; Hamamatsu). Raw images
647 were reconstructed using the Nikon Elements image stack reconstruction algorithm. Images
648 were processed in FIJI⁶⁴. Figures were made in Adobe Illustrator. A minimum of three biological
649 replicates were performed for each experiment unless otherwise noted. All images presented in
650 figures are max projections.

651

652 *IN/OUT cilia assay*

653 RPE1 D21, T21, and Q21 cells stably expressing pHluorin-Smoothed (pLVX-pHluorin-

654 Smoothened vector was a gift from Dr. Derek Toomre) were plated on collagen-coated
655 coverslips, fixed and stained as described in³². Briefly, culture media was removed, cells were
656 gently washed in PBS, and then fixed in 4% PFA in PBS for 10 minutes. Cells were then
657 blocked in 5% normal donkey serum in PBS for 30 minutes followed by incubation with anti-GFP
658 primary antibody solution for 1 hour. Cells were fixed again for 10 minutes, permeabilized with
659 0.1% Triton-X, and incubated in another primary antibody solution containing anti-Actub for 1
660 hour. After gentle washing, cells were incubated with secondary antibodies and Hoechst,
661 followed by washing and mounting on slides.

662

663 *RNAi*

664 Human PCNT siRNA (Smart Pool) (M-012172-01-0005; Dharmacon) was transfected into RPE1
665 cells with Lipofectamine RNAi MAX (13778100; ThermoFisher Scientific) according to the
666 manufacturer's protocol. Mission siRNA universal negative control #1 was used for all negative
667 controls (SIC001-1NMOL; Sigma). All siRNAs were used at a final concentration of 25 nM. Cells
668 were treated with siRNA in serum depleted media for 24 hours before fixation and subsequent
669 immunostaining steps.

670

671 *Generation of lentiviral stable cell lines*

672 RPE1 D21, T21, and Q21 lentiviral stable cell lines were generated by transfecting HEK293T
673 cells with lentiviral GFP-EHD1 or pH-Smoothened constructs and lentivirus packaging plasmids
674 using Lipofectamine 2000 (11668-027; Invitrogen). HEK293T media containing virus was
675 collected and added to target cells in the presence of 2mg/mL polybrene. Transduced cells were
676 selected using 10mg/mL puromycin for three days. To induce GFP-EHD1 expression, 0.125
677 mg/mL doxycycline was added to serum depleted media for 24 hours before fixation.

678

679 *Animal Ethics Statement*

680 All procedures involving mice were approved by the Institutional Animal Care and Use
681 Committee (IACUC) at the University of Colorado Anschutz Medical Campus and were
682 performed in accordance with National Institute Guidelines for the care and use of animals in
683 research.

684

685 *Mouse models of Down syndrome*

686 Mouse models were obtained from the NICHD funded Cytogenetic and Down Syndrome Models
687 Resource Jackson Laboratory. These include B6.129S7-Dp(16Lipi-Zbtb21)1Yey/J (Dp16;
688 stock# 013530), B6;129-Dp(10Prmt2-Pdxk)2Yey/J (Dp10; stock# 013529), and B6;129-
689 Dp(17Abcg1-Rrp1b)3Yey/J (Dp17; stock# 013531). Strains were maintained on a standard
690 chow diet and a 14-hour light/10-hour dark cycle. Littermate controls were used.

691

692 *Cerebellar Slice Cultures*

693 Cerebellums were dissected out of postnatal day 4 pups in ice cold Hank's media and sliced
694 300 μm thick on a tissue chopper.⁶⁵ Slices were transferred to MilliCell filter inserts (Millipore
695 PICM03050) only taking intact slices with at least 5 folia. Excess Hank's was removed from
696 filters and replaced with serum free Neurobasal media supplemented with 1% N2, 0.5%
697 Penicillin/Streptomycin, 0.25% L-glutamine, and 10 mM HEPES. Cerebellar slices were cultured
698 at 37°C and 5% CO₂ and media was changed 8 hours after plating. Slices were grown for 48
699 hours before addition of 500 μm control or PCNT siRNA (D-001910-10-05 Accell Non-targeting
700 Pool; Accell Mouse Pcnt 18541 siRNA—SMARTpool) and then cultured for an additional 48
701 hours before fixation with 4% PFA and staining as described above.

702

703 *Mouse brain immunohistochemistry*

704 Experiments were blinded to gender. P4 pups were anesthetized with Isoflurane before
705 decapitation. Tail clips were used for genotyping. Brains were dissected out and fixed in 4%

706 PFA in PBS overnight at 4°C. Brains were then moved to 30% sucrose in PBS for 1-2 days at
707 4°C. Fixed brains were sliced through the midline; each half was embedded in OCT, frozen on
708 dry ice for ~15 minutes, then stored at -80°C until ready to section. To section, blocks were
709 mounted in OCT and 20 µm sagittal sections were cut using a Leica CM 1950 cryostat
710 microtome. Sections were placed on FisherBrand charged slides (Cat # 12-550-15) and stained
711 on slides as described above.

712

713 *Genotyping*

714 Tissue from Dp10 animals or MEFs were lysed by placing tail clips or heads in Gitschiers Buffer
715 (67 mM Tris pH 8.8, 0.166 mM Ammonium sulfate, 6.7 mM magnesium chloride, 0.005%
716 TritonX, 0.1 mg/ml Proteinase K in water) for 2 hours at 55°C then 95°C for 10 minutes. Tissue
717 from Dp16 or Dp17 animals or MEFs were lysed by placing tail clips or heads in 50 mM sodium
718 hydroxide and heating at 98°C for 2 hours before neutralizing with 1M Tris pH 8 (1:10). Lysed
719 tissue was used for PCR and the resulting banding pattern from PCR was used to determine
720 genotype. Genotyping primers are as follows: Dp10For: GGCGAACGTGGCGAGAAA;
721 Dp10Rev: CCTGCTGCCAAGCCATCAG; Dp16For: CTGCCAGCC ACTCTAGCTCT; Dp16Rev:
722 AATTTCTGTGGGGCAAATG; Dp17For: GGAGCCAGGGCTGATGGT; Dp17Rev:
723 CAACGCGGCCTTTTTACG. Primers for Cux2 were used as controls. Cux2For:
724 GGGACATCACCCACCGTAATCTC; Cux2Rev: GACCACTGAGTCTGGCAACACG.

725

726 *Image Analysis*

727 All intensity analysis was performed on max projected images unless otherwise noted. Radial
728 fluorescence intensity was measured using the Radial Profile Extended ImageJ plugin. Briefly,
729 this plugin plots average fluorescence intensity as a function of distance from a user defined
730 centroid. 10 µm diameter ROIs were centered over the brightest pixel of a Gaussian blurred
731 maximum intensity projection of the centrosome defined by PCNT fluorescence. In cells with

732 GT335-labeled centrioles, the centroid was manually centered between the two centrioles.
733 Background was determined per field of view by the mean intensity of an extracellular ROI.
734 Background subtracted radial intensities were summed and normalized to the D21 average.
735 Centrosomal fluorescence intensity was defined as the sum of radial intensities falling within
736 0.0-1.2 μm from the centroid of analysis. Pericentrosomal fluorescence intensity was defined as
737 the sum of radial intensities falling within 1.2-5.0 μm from the centroid of analysis.

738 Whole cell intensities were calculated using the integrated density within cells outlined in
739 ImageJ. Ciliation frequency was measured by counting either DM1a (Figure 1) or ARL13B
740 (Figures 6) and dividing by the number of nuclei per field of view. For ciliation frequency in
741 cultured cerebellar slices, the number of ARL13B cilia was divided by the number of
742 centrosomes per field of view. For ciliation frequency in fixed cerebellar slices, the number of
743 ARL13B cilia was divided by the mean Hoechst intensity per field of view because individual
744 nuclei could not be resolved in the thick slices.

745 For PCNT siRNA experiments, radial MYOVA and PCNT fluorescence intensity was
746 calculated using the same methods as above. For MYOVA radial distribution, all values were
747 divided by the maximum intensity value per cell and normalized to D21 values. Correlation
748 analyses were performed by plotting 10 μm diameter PCNT intensities normalized within a cell
749 line to either centrosomal or pericentrosomal normalized MYOVA intensities. R values and
750 significance were calculated by running a correlation analysis in GraphPad. PCNT levels were
751 analyzed with a 10 μm diameter circle centered on the centrosome to measure the integrated
752 density. Background was determined with an extracellular ROI. Background subtracted values
753 were normalized to the D21 average.

754 GM130 and Golgin97 intensities were measured by drawing an ROI around the GM130
755 or Golgin97 signal and measuring the integrated density within this ROI. Background was
756 determined by an extracellular ROI. Background subtracted values were normalized to the D21
757 average. To quantify early endosome and lysosome levels, integrated density was measured

758 across a field of view and divided by the number of nuclei within the same field of view. Values
759 were normalized to the D21 average.

760 All transition zone antibodies were co-stained with GT335. The transition zone was
761 identified by the gap in GT335 signal between the mother centriole and the base of the cilium.
762 Transition zone protein intensity was determined by centering a 1 μm x 1 μm box over the
763 transition zone and measuring the integrated density. Background was determined by a 1 μm x
764 1 μm box randomly placed near the centrosome. Background subtracted values were
765 normalized to the D21 average. For TMEM67, the ROI was a 0.5 μm x 0.5 μm box to avoid
766 centrosomal TMEM67.

767

768 *Statistical Analysis*

769 All data sets were tested for Normality using D'Agostino and Pearson Omnibus Normality Test
770 in GraphPad Prism 9. Normal data sets were then tested for significance with a two-tailed
771 unpaired t-test and non-normal data sets were tested for significance using the Mann-Whitney
772 test. All graphs show mean \pm SD. All experiments utilized at least three biological replicates,
773 unless otherwise noted.

774

775 *Electron Tomography*

776 RPE1 cells were grown on sapphire discs and prepared for electron microscopy using high
777 pressure freezing and freeze substitution as described in McDonald et al.⁶⁶ Briefly, 3mm
778 sapphire discs (Technotrade International) were coated with gold and a large F was then
779 scratched into the surface to help orient the cell side. The disks were coated with collagen,
780 sterilized under UV light and cells plated for culturing. Monolayers grown on sapphire discs were
781 then frozen using a Wohlwend Compact02 high pressure freezer (Technotrade International).
782 The frozen cells were then freeze substituted in 1% OsO₄ and 0.1% uranyl acetate in acetone
783 at -80°C for 3 days then gradually warmed to room temperature. The discs were then flat

784 embedded in a thin layer of Epon resin and polymerized at 60°C. Regions containing cells were
785 identified in the light microscope, and a small square of resin containing the cells was excised
786 and remounted onto a blank resin block. The cells were then sectioned en face and serial, thick
787 sections (250-300nm) were collected onto formvar-coated slot grids. Grids were post stained
788 with 2% uranyl acetate and Reynold's lead citrate and 15 nm colloidal gold (BBI International)
789 was affixed to the section surface to serve as alignment markers.

790 Tomography was performed using a Tecnai F30 microscope operating at 300 kV
791 (Thermo Fisher Scientific, Waltham, MA). Dual axis tilt series were collected over a +/- 60°
792 range using the SerialEM image acquisition software,⁶⁷ and a Gatan OneView camera (Gatan,
793 Inc., Pleasanton, CA). For most data sets, tilt series were collected from 2-4 serial sections to
794 reconstruct a larger volume of cell data. Tomograms were computed, serial tomograms joined
795 and cellular features were modeled using the IMOD 4.9 software package
796 (<https://bio3d.colorado.edu/imod/>).^{68,69}

797 Organelles at the centrosomes of the cells (centrioles, vesicles, positions of MT and their
798 ends) were manually traced in these reconstructions using the 3dmod program in the IMOD
799 software package.⁶⁸ Models were projected in 3D to show the arrangement of the centrioles,
800 vesicles, microtubules and the position their ends within the volume. In total, 4 centrosomes
801 from D21, 3 centrosomes from T21, and 4 centrosomes from Q21 were reconstructed and
802 modeled. The modeled centrosomes came from different stages, including at or before ciliary
803 vesicle formation, and one D21 and T21 set with a primary cilium.

804

805 **Supplemental Figure Legends**

806 *Figure S1.* (A-C) Quantitation of whole cell PCNT intensities for D21 (A), T21 (B), and Q21 (C)
807 cells throughout the time course normalized to average at 0 h. Graph shows mean \pm SD. (D)
808 Quantitation of centrosomal PCNT intensities in a 0-1.2 μ m radial circle around the centrosome
809 throughout the time course normalized to D21 average at 0 h. Graph shows mean \pm SD. (E)
810 Quantitation of pericentrosomal PCNT intensities in a 1.2-5 μ m radial circle around the
811 centrosome throughout the time course normalized to D21 average at 0 h. Graph shows mean \pm
812 SD. (F) Quantitation of centrosomal microtubule intensities in a 0-1.2 μ m radial circle around the
813 centrosome throughout the time course normalized to D21 average at 0 h. Graph shows mean \pm
814 SD. (G) Quantitation of pericentrosomal microtubule intensities in a 1.2-5 μ m radial circle
815 around the centrosome throughout the time course normalized to D21 average at 0 h. Graph
816 shows mean \pm SD. N's and statistical tests are listed in Table S1.

817

818 *Figure S2.* (A, B) Representative SIM images of RPE1 D21, T21, and Q21 cells grown on
819 coverslips and serum depleted for 24 h. Cells were stained with GT335 and the distal
820 appendage marker CEP83 (A) or centrin, Acetylated tubulin (Actub), and the subdistal
821 appendage marker Ninein (NIN) (B). Percentages represent cells with indicated marker for 3
822 N's.

823

824 *Figure S3.* (A) Quantitation of whole cell MYOVA intensity for D21, T21, and Q21 cells. (B-D)
825 Distribution of centrosomal MYOVA intensities moving away from the centrosome for 2 (B), 4
826 (C), and 24 (D) h timepoints. Values were normalized to the D21 average. Graph shows mean \pm
827 SD. (E) Representative SIM images of RPE1 D21, T21, and Q21 cells grown on coverslips and
828 serum depleted for 24 h. Cells were either treated with control or PCNT siRNA during the 24 h
829 serum depletion. Cells were stained with GT335 and MYOVA. (F) Quantitation of PCNT
830 intensities in a 5 μ m radial circle around the centrosome in control and PCNT siRNA treated

831 cells normalized to the D21 average. Graph shows mean \pm SD. (G, H) Correlation analysis
832 between PCNT and MYOVA levels for D21, T21, and Q21 cells 24 h after serum depletion. (I)
833 Representative confocal images of RPE1 D21, T21, and Q21 cells stably expressing GFP-
834 EHD1 grown on coverslips and serum depleted for 24 h. Cells were stained for PCNT and
835 Actub. N's and statistical tests are listed in Table S1.

836

837 *Figure S4.* (A) Quantitation of CP110 centriole capping for D21, T21, and Q21 cells 24 h after
838 serum depletion. (B) Representative SIM images of RPE1 D21, T21, and Q21 cells grown on
839 coverslips and serum depleted for 24 h. Cells were stained with GT335 and the centriole
840 capping protein CEP97. Percentages represent cells with indicated phenotype across 3 N's. (C)
841 Quantitation of CEP97 centriole capping for D21, T21, and Q21 cells. (D) Representative SIM
842 images of RPE1 D21, T21, and Q21 cells grown on coverslips and serum depleted for 2, 4, 8,
843 24, and 48 h. Cells were stained with γ -tubulin, Actub, and RAB8. Percentages represent cells
844 with indicated phenotype across 3 N's. (E) Representative confocal images of RPE1 D21, T21,
845 and Q21 cells grown on coverslips and serum depleted for 24 h. Cells were stained with
846 Hoechst, PCNT, Golgin97, and RAB8. (F) Quantitation of RAB8 Golgi intensity normalized to
847 the D21 average. (G) Cartoon model depicting intracellular trafficking pathways. (H)
848 Representative confocal images of RPE1 D21, T21, and Q21 cells grown on coverslips and
849 serum depleted for 24 h. Cells were stained with Hoechst, γ -tubulin, and the cis-Golgi marker
850 GM130. (I-J) Quantitation of GM130 intensity (I) and GM130-labeled Golgi area (J) normalized
851 to the D21 average. (K) Representative confocal images of RPE1 D21, T21, and Q21 cells
852 grown on coverslips and serum depleted for 24 h. Cells were stained with Hoechst, PCNT, and
853 the trans-Golgi marker Golgin97. (L-M) Quantitation of Golgin97 intensity (L) and Golgin97-
854 labeled Golgi area (M) normalized to the D21 average. (N) Representative confocal images of
855 RPE1 D21, T21, and Q21 cells grown on coverslips and serum depleted for 24 h. Cells were

856 stained with Hoechst, γ -tubulin, and the early endosome marker EEA1. (O) Quantitation of
857 EEA1 intensity normalized to the D21 average. (P) Representative confocal images of RPE1
858 D21, T21, and Q21 cells grown on coverslips and serum depleted for 24 h. Cells were stained
859 with Hoechst, PCNT, and the lysosome marker CD63. Q) Quantitation of CD63 intensity
860 normalized to the D21 average. Graphs shows mean \pm SD. N's and statistical tests are listed in
861 Table S1.

862

863 *Figure S5.* (A) Representative confocal images of RPE1 D21 and T21 cells stably expressing
864 pH-Smoothed (pH-SMO) grown on coverslips and serum depleted for 24 h. The IN/OUT
865 assay was performed, and cells were stained with an anti-GFP antibody pre-permeabilization
866 and Actub after. Anti-GFP labeled cilia are extracellular. (B) Quantitation of extracellular cilia in
867 D21 and T21 cells. (C) Quantitation of centrosomal CEP290 intensity in 0-1.2 μ m region around
868 centrosome.

869

870 *Figure S6.* For all following experiments, WT and Dp primary MEFs were isolated from E12.5
871 dams, grown on coverslips, and serum depleted for 24 h. (A, B) Representative confocal images
872 of WT and Dp16 (A) or Dp17 (B) MEFs. Cells were stained with Hoechst, the ciliary marker
873 ARL13B, and γ -tubulin. (C, D) Representative confocal images of WT and Dp16 (C) or Dp17 (D)
874 MEFs. Cells were stained with PCNT and ARL13B. (E) Representative confocal images of WT
875 and the Dp10-2 MEF line that does not have decreased cilia. Cells were stained with Hoechst,
876 the ciliary marker ARL13B, and Actub. (F) Quantitation of the number of cells with a primary
877 cilium in WT and Dp10-2 MEFs. (G) Quantitation of PCNT intensities in a 5 μ m radial circle
878 around the centrosome in WT and Dp10-2 MEFs. Values were normalized to the WT average.
879 (H) Quantitation of ciliary SMO levels in SAG-treated cells for WT and Dp10-2 MEFs. Values

880 were normalized to the WT average. Graphs show mean \pm SD. N's and statistical tests are
881 listed in Table S1.

882

883 *Figure S7.* (A) Representative tiled confocal images of WT and Dp10 P4 animals corresponding
884 to the same cerebellar folia in each animal. Brain sections were stained with Hoechst and the
885 cell proliferation marker Ki67. (B) Quantitation of the number of Ki67-positive cells in the
886 external granular layer of WT and Dp10 animals. (C) Representative tiled confocal images of
887 WT and Dp10 P4 animals corresponding to the same cerebellar folia in each animal. Brain
888 sections were stained with Hoechst and the Purkinje cell marker calbindin (CALB1) and the
889 microtubule binding protein doublecortin (DCX). The far-right panel shows insets of DCX
890 staining. (D-F) Representative tiled confocal images of multiciliated ependymal cells lining the
891 ventricle next to the cerebellum from P4 wild-type (WT) and Dp10 (E), Dp16 (F), and Dp17 (G)
892 animals. Brain sections were stained with Hoechst, ARL13B, and γ -tubulin.

893

894 *Video S1-3.* Movies of D21 (S1), T21 (S2), and Q21 (S3) cells from Figure 2 showing the EM
895 tomogram volume, then models projecting from the images, then the model turning without
896 images. Mother centriole (yellow), daughter centriole (magenta), microtubule minus ends (light
897 blue spheres), microtubules (green), and vesicles (red). Note the proximity of vesicles to
898 microtubules.

899

900 **References**

- 901 1 Haydar, T. F. & Reeves, R. H. Trisomy 21 and early brain development. *Trends Neurosci*
902 **35**, 81-91, doi:10.1016/j.tins.2011.11.001 (2012).
- 903 2 Bergström, S. *et al.* Trends in Congenital Heart Defects in Infants With Down Syndrome.
904 *Pediatrics* **138**, doi:10.1542/peds.2016-0123 (2016).
- 905 3 Richtsmeier, J. T., Baxter, L. L. & Reeves, R. H. Parallels of craniofacial maldevelopment
906 in Down syndrome and Ts65Dn mice. *Developmental dynamics : an official publication*
907 *of the American Association of Anatomists* **217**, 137-145, doi:10.1002/(sici)1097-
908 0177(200002)217:2<137::Aid-dvdy1>3.0.Co;2-n (2000).
- 909 4 Goetz, S. C. & Anderson, K. V. The primary cilium: a signalling centre during vertebrate
910 development. *Nat Rev Genet* **11**, 331-344, doi:10.1038/nrg2774 (2010).
- 911 5 Schmidt, K. N. *et al.* Cep164 mediates vesicular docking to the mother centriole during
912 early steps of ciliogenesis. *J Cell Biol* **199**, 1083-1101, doi:10.1083/jcb.201202126 (2012).
- 913 6 Tanos, B. E. *et al.* Centriole distal appendages promote membrane docking, leading to
914 cilia initiation. *Genes Dev* **27**, 163-168, doi:10.1101/gad.207043.112 (2013).
- 915 7 Ishikawa, H., Kubo, A., Tsukita, S. & Tsukita, S. Odf2-deficient mother centrioles lack
916 distal/subdistal appendages and the ability to generate primary cilia. *Nat Cell Biol* **7**,
917 517-524, doi:10.1038/ncb1251 (2005).
- 918 8 Wu, C. T., Chen, H. Y. & Tang, T. K. Myosin-Va is required for preciliary vesicle
919 transportation to the mother centriole during ciliogenesis. *Nat Cell Biol* **20**, 175-185,
920 doi:10.1038/s41556-017-0018-7 (2018).
- 921 9 Lu, Q. *et al.* Early steps in primary cilium assembly require EHD1/EHD3-dependent ciliary
922 vesicle formation. *Nat Cell Biol* **17**, 228-240, doi:10.1038/ncb3109 (2015).
- 923 10 Garcia-Gonzalo, F. R. & Reiter, J. F. Scoring a backstage pass: mechanisms of ciliogenesis
924 and ciliary access. *J Cell Biol* **197**, 697-709, doi:10.1083/jcb.201111146 (2012).
- 925 11 Sung, C. H. & Leroux, M. R. The roles of evolutionarily conserved functional modules in
926 cilia-related trafficking. *Nat Cell Biol* **15**, 1387-1397, doi:10.1038/ncb2888 (2013).
- 927 12 Nachury, M. V., Seeley, E. S. & Jin, H. Trafficking to the ciliary membrane: how to get
928 across the periciliary diffusion barrier? *Annu Rev Cell Dev Biol* **26**, 59-87,
929 doi:10.1146/annurev.cellbio.042308.113337 (2010).
- 930 13 Kim, J., Krishnaswami, S. R. & Gleeson, J. G. CEP290 interacts with the centriolar satellite
931 component PCM-1 and is required for Rab8 localization to the primary cilium. *Hum Mol*
932 *Genet* **17**, 3796-3805, doi:10.1093/hmg/ddn277 (2008).
- 933 14 Blacque, O. E., Scheidel, N. & Kuhns, S. Rab GTPases in cilium formation and function.
934 *Small GTPases* **9**, 76-94, doi:10.1080/21541248.2017.1353847 (2018).
- 935 15 Hori, A. & Toda, T. Regulation of centriolar satellite integrity and its physiology. *Cell Mol*
936 *Life Sci* **74**, 213-229, doi:10.1007/s00018-016-2315-x (2017).
- 937 16 Doxsey, S. J., Stein, P., Evans, L., Calarco, P. D. & Kirschner, M. Pericentrin, a highly
938 conserved centrosome protein involved in microtubule organization. *Cell* **76**, 639-650,
939 doi:10.1016/0092-8674(94)90504-5 (1994).
- 940 17 Gavilan, M. P. *et al.* The dual role of the centrosome in organizing the microtubule
941 network in interphase. *EMBO Rep* **19**, doi:10.15252/embr.201845942 (2018).

- 942 18 Martinez-Campos, M., Basto, R., Baker, J., Kernan, M. & Raff, J. W. The *Drosophila*
943 pericentrin-like protein is essential for cilia/flagella function, but appears to be
944 dispensable for mitosis. *J Cell Biol* **165**, 673-683, doi:10.1083/jcb.200402130 (2004).
- 945 19 Galati, D. F., Sullivan, K. D., Pham, A. T., Espinosa, J. M. & Pearson, C. G. Trisomy 21
946 Represses Cilia Formation and Function. *Dev Cell* **46**, 641-650.e646,
947 doi:10.1016/j.devcel.2018.07.008 (2018).
- 948 20 McCurdy, B. L. *et al.* Trisomy 21 increases microtubules and disrupts centriolar satellite
949 localization. *bioRxiv* (2021).
- 950 21 Joo, K. *et al.* CCDC41 is required for ciliary vesicle docking to the mother centriole. *Proc*
951 *Natl Acad Sci U S A* **110**, 5987-5992, doi:10.1073/pnas.1220927110 (2013).
- 952 22 Shakya, S. & Westlake, C. J. Recent advances in understanding assembly of the primary
953 cilium membrane. *Fac Rev* **10**, 16, doi:10.12703/r/10-16 (2021).
- 954 23 Yang, T. T. *et al.* Super-resolution architecture of mammalian centriole distal
955 appendages reveals distinct blade and matrix functional components. *Nat Commun* **9**,
956 2023, doi:10.1038/s41467-018-04469-1 (2018).
- 957 24 Lange, B. M. & Gull, K. A molecular marker for centriole maturation in the mammalian
958 cell cycle. *J Cell Biol* **130**, 919-927, doi:10.1083/jcb.130.4.919 (1995).
- 959 25 Nakagawa, Y., Yamane, Y., Okanoue, T., Tsukita, S. & Tsukita, S. Outer dense fiber 2 is a
960 widespread centrosome scaffold component preferentially associated with mother
961 centrioles: its identification from isolated centrosomes. *Mol Biol Cell* **12**, 1687-1697,
962 doi:10.1091/mbc.12.6.1687 (2001).
- 963 26 Mogensen, M. M., Malik, A., Piel, M., Bouckson-Castaing, V. & Bornens, M. Microtubule
964 minus-end anchorage at centrosomal and non-centrosomal sites: the role of ninein. *J*
965 *Cell Sci* **113 (Pt 17)**, 3013-3023 (2000).
- 966 27 Spektor, A., Tsang, W. Y., Khoo, D. & Dynlacht, B. D. Cep97 and CP110 suppress a cilia
967 assembly program. *Cell* **130**, 678-690, doi:10.1016/j.cell.2007.06.027 (2007).
- 968 28 Liu, M. *et al.* NudCL2 is an autophagy receptor that mediates selective autophagic
969 degradation of CP110 at mother centrioles to promote ciliogenesis. *Cell Res*,
970 doi:10.1038/s41422-021-00560-3 (2021).
- 971 29 Nachury, M. V. *et al.* A Core Complex of BBS Proteins Cooperates with the GTPase Rab8
972 to Promote Ciliary Membrane Biogenesis. *Cell* **129**, 1201-1213,
973 doi:10.1016/j.cell.2007.03.053 (2007).
- 974 30 Moritz, O. L. *et al.* Mutant rab8 Impairs docking and fusion of rhodopsin-bearing post-
975 Golgi membranes and causes cell death of transgenic *Xenopus* rods. *Mol Biol Cell* **12**,
976 2341-2351, doi:10.1091/mbc.12.8.2341 (2001).
- 977 31 Sorokin, S. CENTRIOLES AND THE FORMATION OF RUDIMENTARY CILIA BY FIBROBLASTS
978 AND SMOOTH MUSCLE CELLS. *J Cell Biol* **15**, 363, doi:10.1083/jcb.15.2.363 (1962).
- 979 32 Kukic, I., Rivera-Molina, F. & Toomre, D. The IN/OUT assay: a new tool to study
980 ciliogenesis. *Cilia* **5**, 23, doi:10.1186/s13630-016-0044-2 (2016).
- 981 33 Tobin, J. L. & Beales, P. L. The nonmotile ciliopathies. *Genet Med* **11**, 386-402,
982 doi:10.1097/GIM.0b013e3181a02882 (2009).
- 983 34 Sang, L. *et al.* Mapping the NPHP-JBTS-MKS protein network reveals ciliopathy disease
984 genes and pathways. *Cell* **145**, 513-528, doi:10.1016/j.cell.2011.04.019 (2011).

- 985 35 Craige, B. *et al.* CEP290 tethers flagellar transition zone microtubules to the membrane
986 and regulates flagellar protein content. *J Cell Biol* **190**, 927-940,
987 doi:10.1083/jcb.201006105 (2010).
- 988 36 Yang, T. T. *et al.* Superresolution Pattern Recognition Reveals the Architectural Map of
989 the Ciliary Transition Zone. *Sci Rep* **5**, 14096, doi:10.1038/srep14096 (2015).
- 990 37 Williams, C. L. *et al.* MKS and NPHP modules cooperate to establish basal
991 body/transition zone membrane associations and ciliary gate function during
992 ciliogenesis. *J Cell Biol* **192**, 1023-1041, doi:10.1083/jcb.201012116 (2011).
- 993 38 Garcia-Gonzalo, F. R. *et al.* A transition zone complex regulates mammalian ciliogenesis
994 and ciliary membrane composition. *Nat Genet* **43**, 776-784, doi:10.1038/ng.891 (2011).
- 995 39 Roper, R. J. *et al.* Defective cerebellar response to mitogenic Hedgehog signaling in
996 Down [corrected] syndrome mice. *Proc Natl Acad Sci U S A* **103**, 1452-1456,
997 doi:10.1073/pnas.0510750103 (2006).
- 998 40 Gupta, M., Dhanasekaran, A. R. & Gardiner, K. J. Mouse models of Down syndrome:
999 gene content and consequences. *Mamm Genome* **27**, 538-555, doi:10.1007/s00335-
1000 016-9661-8 (2016).
- 1001 41 Yu, T. *et al.* Effects of individual segmental trisomies of human chromosome 21 syntenic
1002 regions on hippocampal long-term potentiation and cognitive behaviors in mice. *Brain*
1003 *Research* **1366**, 162-171, doi:10.1016/j.brainres.2010.09.107 (2010).
- 1004 42 van Dam, T. J., Wheway, G., Slaats, G. G., Huynen, M. A. & Giles, R. H. The SYSCILIA gold
1005 standard (SCGSv1) of known ciliary components and its applications within a systems
1006 biology consortium. *Cilia* **2**, 7, doi:10.1186/2046-2530-2-7 (2013).
- 1007 43 Kong, J. H., Siebold, C. & Rohatgi, R. Biochemical mechanisms of vertebrate hedgehog
1008 signaling. *Development* **146**, doi:10.1242/dev.166892 (2019).
- 1009 44 Ho, E. K. & Stearns, T. Hedgehog signaling and the primary cilium: implications for
1010 spatial and temporal constraints on signaling. *Development* **148**,
1011 doi:10.1242/dev.195552 (2021).
- 1012 45 Smeyne, R. J. *et al.* Local control of granule cell generation by cerebellar Purkinje cells.
1013 *Mol Cell Neurosci* **6**, 230-251, doi:10.1006/mcne.1995.1019 (1995).
- 1014 46 Wechsler-Reya, R. J. & Scott, M. P. Control of neuronal precursor proliferation in the
1015 cerebellum by Sonic Hedgehog. *Neuron* **22**, 103-114, doi:10.1016/s0896-6273(00)80682-
1016 0 (1999).
- 1017 47 Spassky, N. *et al.* Primary cilia are required for cerebellar development and Shh-
1018 dependent expansion of progenitor pool. *Dev Biol* **317**, 246-259,
1019 doi:10.1016/j.ydbio.2008.02.026 (2008).
- 1020 48 Haldipur, P. *et al.* Preterm delivery disrupts the developmental program of the
1021 cerebellum. *PLOS ONE* **6**, e23449, doi:10.1371/journal.pone.0023449 (2011).
- 1022 49 Nguyen, V. *et al.* Sonic Hedgehog Agonist Protects Against Complex Neonatal Cerebellar
1023 Injury. *Cerebellum* **17**, 213-227, doi:10.1007/s12311-017-0895-0 (2018).
- 1024 50 Delaval, B. & Doxsey, S. J. Pericentrin in cellular function and disease. *J Cell Biol* **188**,
1025 181-190, doi:10.1083/jcb.200908114 (2010).
- 1026 51 Endoh-Yamagami, S. *et al.* A mutation in the pericentrin gene causes abnormal
1027 interneuron migration to the olfactory bulb in mice. *Dev Biol* **340**, 41-53,
1028 doi:10.1016/j.ydbio.2010.01.017 (2010).

- 1029 52 Gleeson, J. G., Lin, P. T., Flanagan, L. A. & Walsh, C. A. Doublecortin is a microtubule-
1030 associated protein and is expressed widely by migrating neurons. *Neuron* **23**, 257-271,
1031 doi:10.1016/s0896-6273(00)80778-3 (1999).
- 1032 53 Francis, F. *et al.* Doublecortin is a developmentally regulated, microtubule-associated
1033 protein expressed in migrating and differentiating neurons. *Neuron* **23**, 247-256,
1034 doi:10.1016/s0896-6273(00)80777-1 (1999).
- 1035 54 Nishita, M., Satake, T., Minami, Y. & Suzuki, A. Regulatory mechanisms and cellular
1036 functions of non-centrosomal microtubules. *J Biochem* **162**, 1-10,
1037 doi:10.1093/jb/mvx018 (2017).
- 1038 55 Hibbard, J. V. K., Vazquez, N., Satija, R. & Wallingford, J. B. Protein turnover dynamics
1039 suggest a diffusion-to-capture mechanism for peri-basal body recruitment and retention
1040 of intraflagellar transport proteins. *Mol Biol Cell*, mbcE20110717, doi:10.1091/mbc.E20-
1041 11-0717 (2021).
- 1042 56 Duchon, A. *et al.* Identification of the translocation breakpoints in the Ts65Dn and
1043 Ts1Cje mouse lines: relevance for modeling Down syndrome. *Mamm Genome* **22**, 674-
1044 684, doi:10.1007/s00335-011-9356-0 (2011).
- 1045 57 Stemm-Wolf, A. J., O'Toole, E. T., Sheridan, R. M., Morgan, J. T. & Pearson, C. G. The SON
1046 RNA splicing factor is required for intracellular trafficking structures that promote
1047 centriole assembly and ciliogenesis. *Mol Biol Cell*, mbcE21060305,
1048 doi:10.1091/mbc.E21-06-0305 (2021).
- 1049 58 Ahn, E. Y. *et al.* SON controls cell-cycle progression by coordinated regulation of RNA
1050 splicing. *Mol Cell* **42**, 185-198, doi:10.1016/j.molcel.2011.03.014 (2011).
- 1051 59 Yu, T. *et al.* A mouse model of Down syndrome trisomic for all human chromosome 21
1052 syntenic regions. *Hum Mol Genet* **19**, 2780-2791, doi:10.1093/hmg/ddq179 (2010).
- 1053 60 Del Viso, F. *et al.* Congenital Heart Disease Genetics Uncovers Context-Dependent
1054 Organization and Function of Nucleoporins at Cilia. *Dev Cell* **38**, 478-492,
1055 doi:10.1016/j.devcel.2016.08.002 (2016).
- 1056 61 Lane, A. A. *et al.* Triplication of a 21q22 region contributes to B cell transformation
1057 through HMG1N1 overexpression and loss of histone H3 Lys27 trimethylation. *Nat Genet*
1058 **46**, 618-623, doi:10.1038/ng.2949 (2014).
- 1059 62 Mariani, L. E. *et al.* Arl13b regulates Shh signaling from both inside and outside the
1060 cilium. *Mol Biol Cell* **27**, 3780-3790, doi:10.1091/mbc.E16-03-0189 (2016).
- 1061 63 Waterman-Storer, C. M. & Salmon, E. D. Actomyosin-based retrograde flow of
1062 microtubules in the lamella of migrating epithelial cells influences microtubule dynamic
1063 instability and turnover and is associated with microtubule breakage and treadmilling. *J*
1064 *Cell Biol* **139**, 417-434, doi:10.1083/jcb.139.2.417 (1997).
- 1065 64 Schindelin, J. *et al.* Fiji: an open-source platform for biological-image analysis. *Nat*
1066 *Methods* **9**, 676-682, doi:10.1038/nmeth.2019 (2012).
- 1067 65 Liu, Y. *et al.* Myelin-specific multiple sclerosis antibodies cause complement-dependent
1068 oligodendrocyte loss and demyelination. *Acta Neuropathol Commun* **5**, 25,
1069 doi:10.1186/s40478-017-0428-6 (2017).
- 1070 66 McDonald, K. *et al.* "Tips and tricks" for high-pressure freezing of model systems.
1071 *Methods in cell biology* **96**, 671-693, doi:10.1016/s0091-679x(10)96028-7 (2010).

- 1072 67 Mastronarde, D. N. Automated electron microscope tomography using robust prediction
1073 of specimen movements. *J Struct Biol* **152**, 36-51, doi:10.1016/j.jsb.2005.07.007 (2005).
1074 68 Kremer, J. R., Mastronarde, D. N. & McIntosh, J. R. Computer visualization of three-
1075 dimensional image data using IMOD. *J Struct Biol* **116**, 71-76,
1076 doi:10.1006/jsbi.1996.0013 (1996).
1077 69 Mastronarde, D. N. Dual-axis tomography: an approach with alignment methods that
1078 preserve resolution. *J Struct Biol* **120**, 343-352, doi:10.1006/jsbi.1997.3919 (1997).
1079

Figure 1

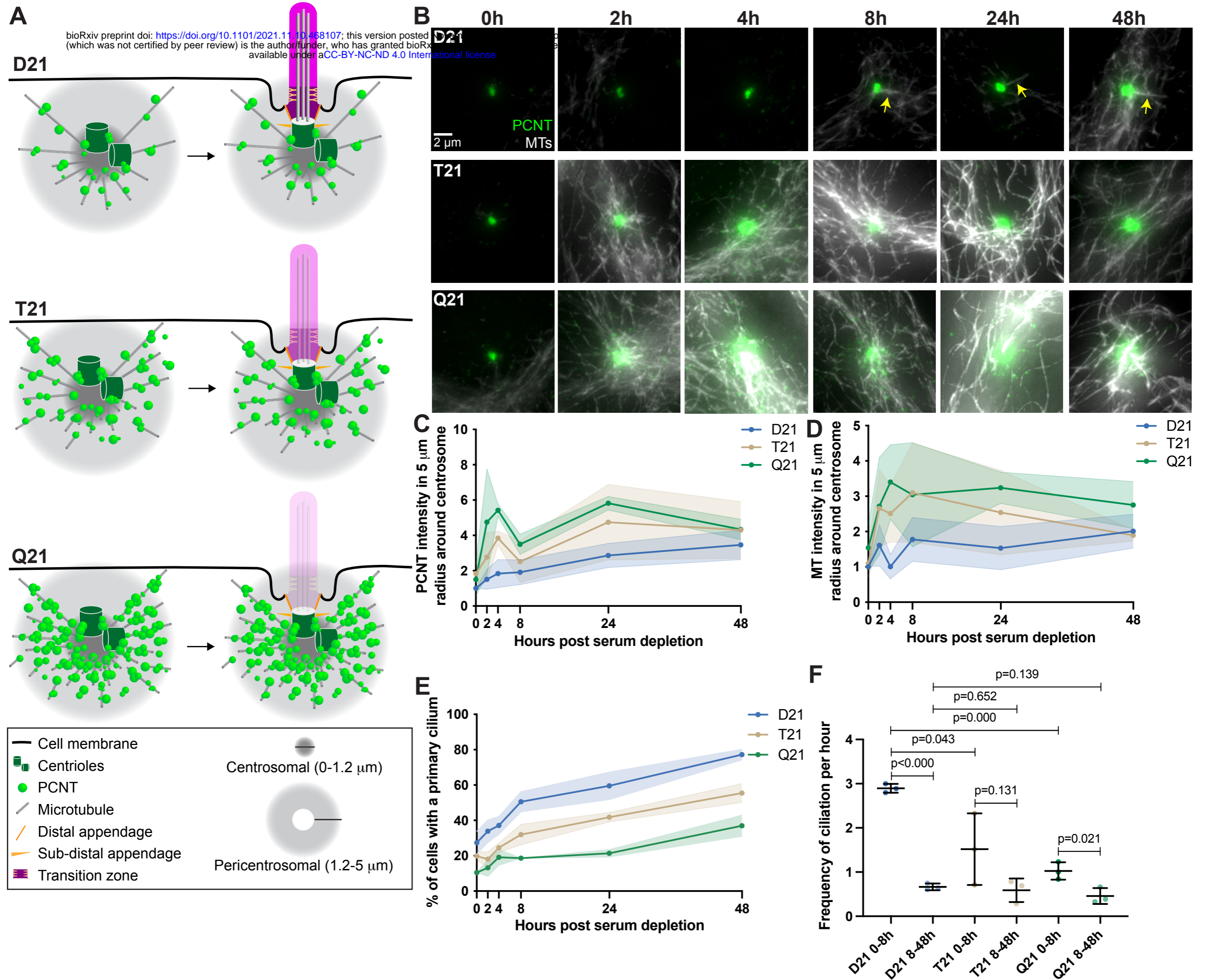


Figure 2

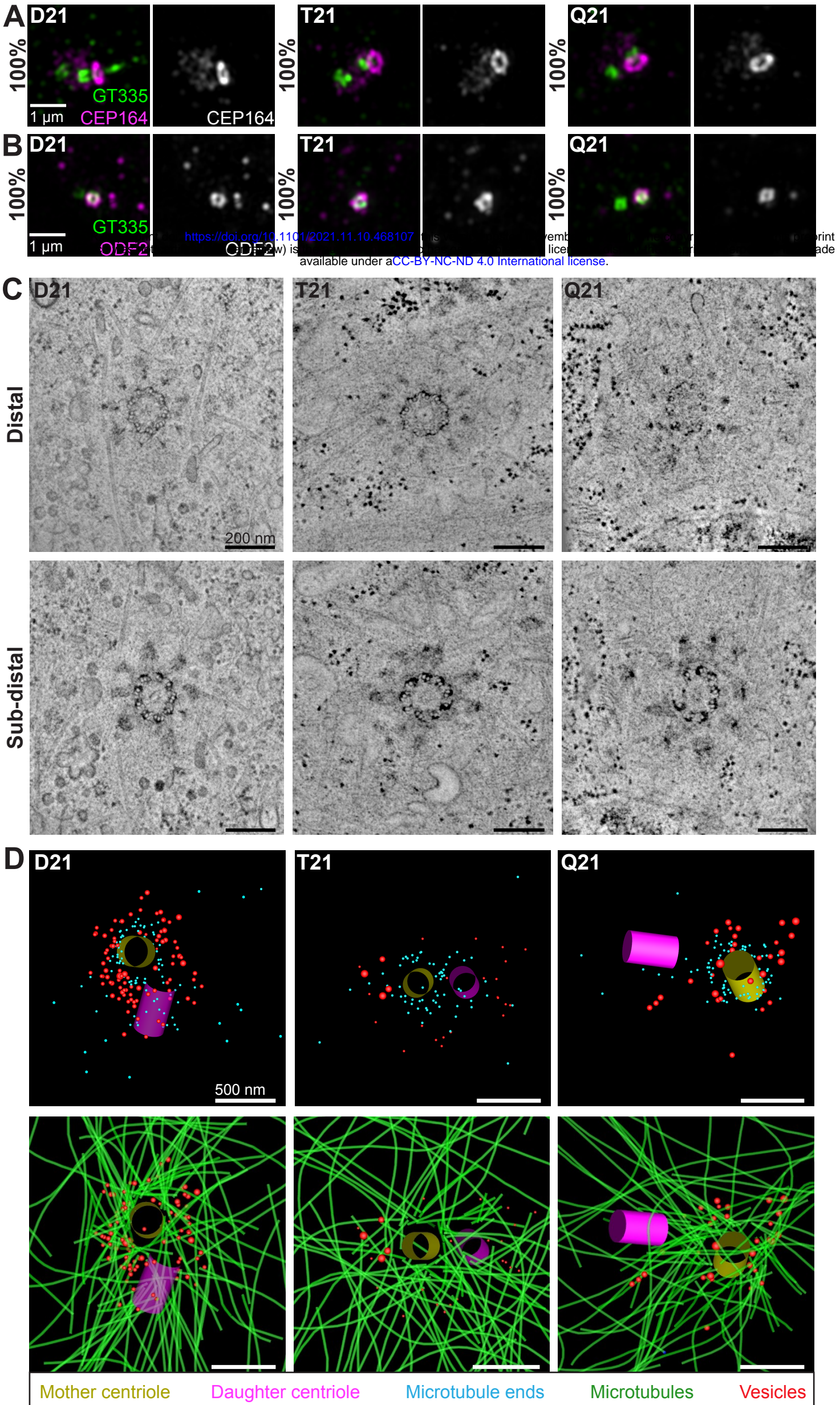
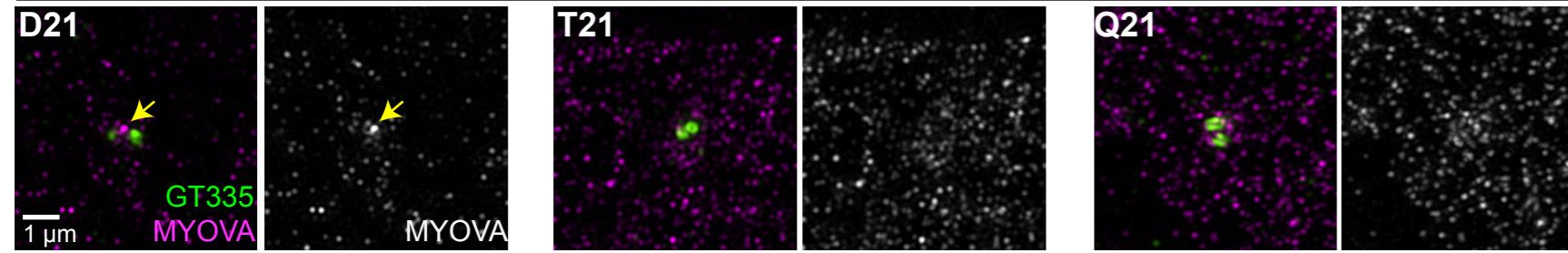
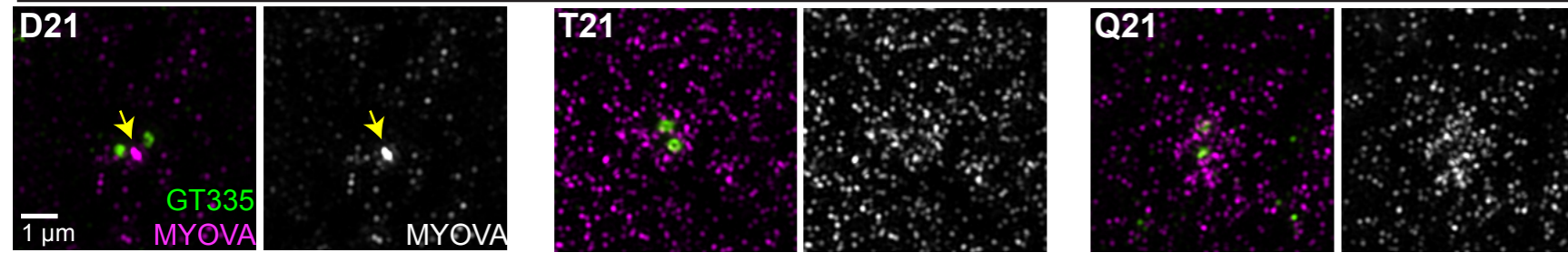


Figure 3**A**

2h serum depletion



4h serum depletion



24h serum depletion

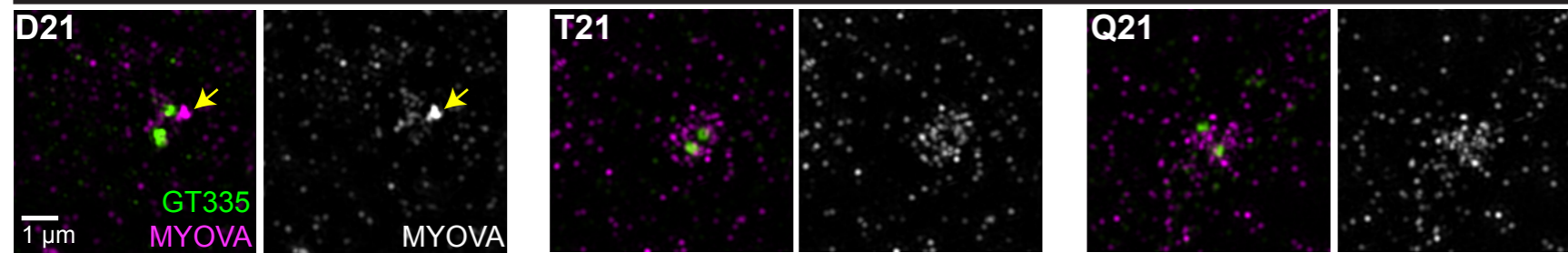
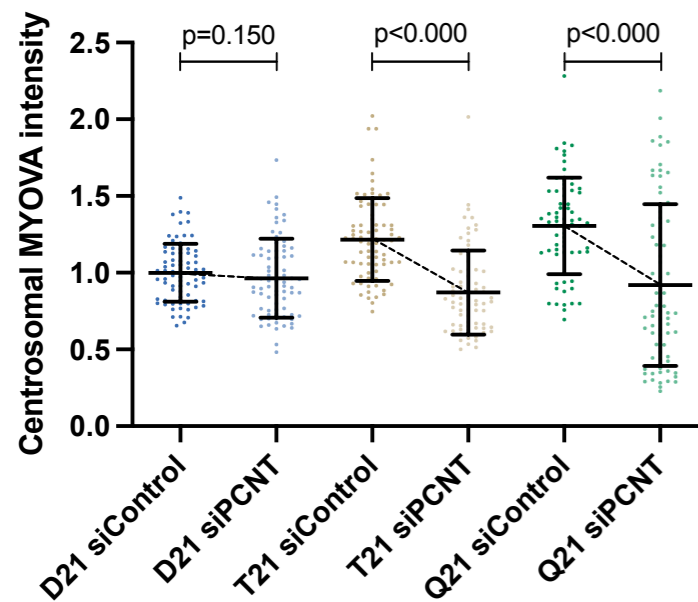
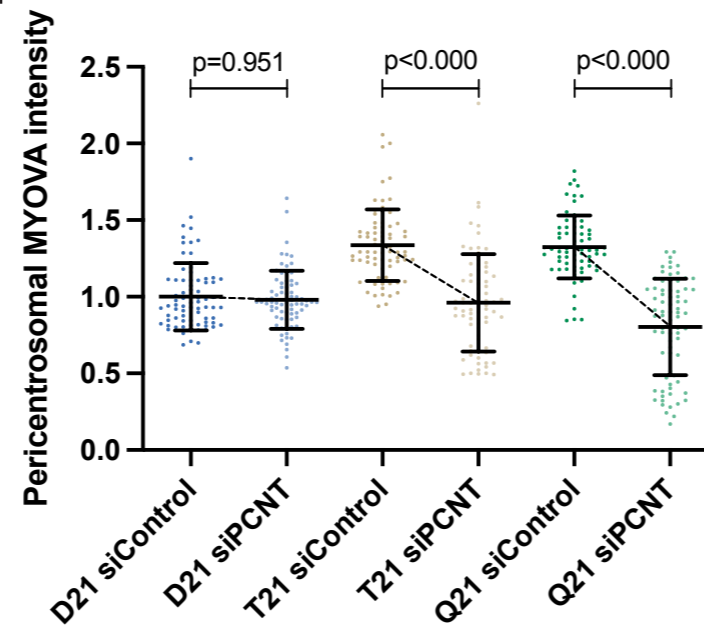
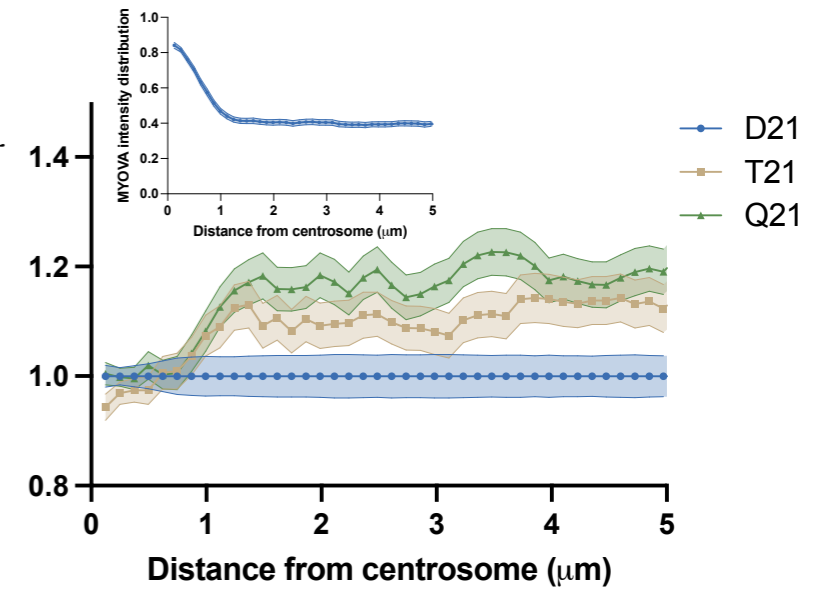
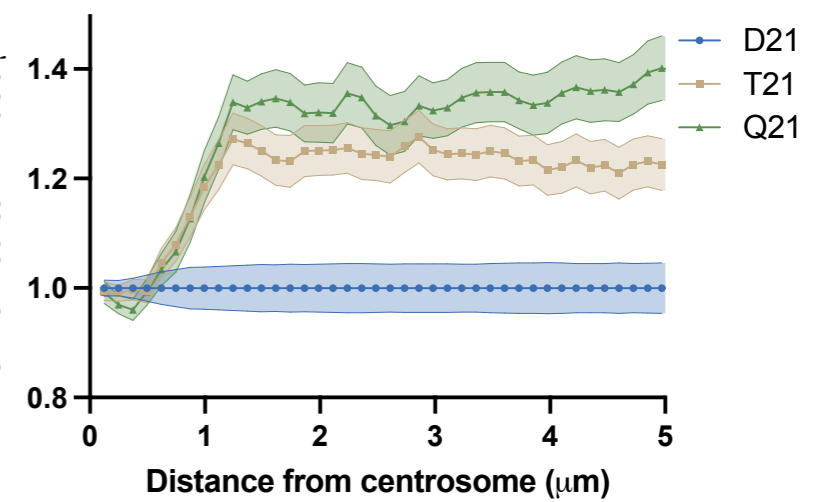
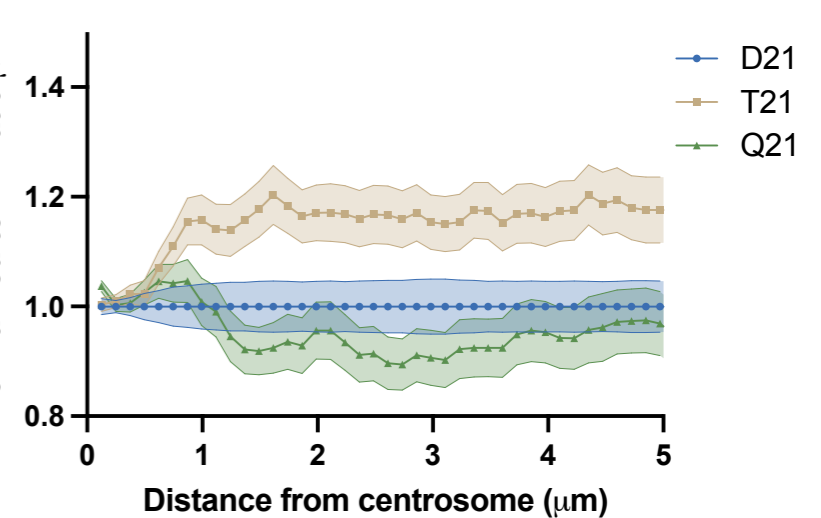
**E****F****B**MYOVA intensity distribution
normalized to D21 at 0 μm**C**MYOVA intensity distribution
normalized to D21 at 0 μm**D**MYOVA intensity distribution
normalized to D21 at 0 μm

Figure 4

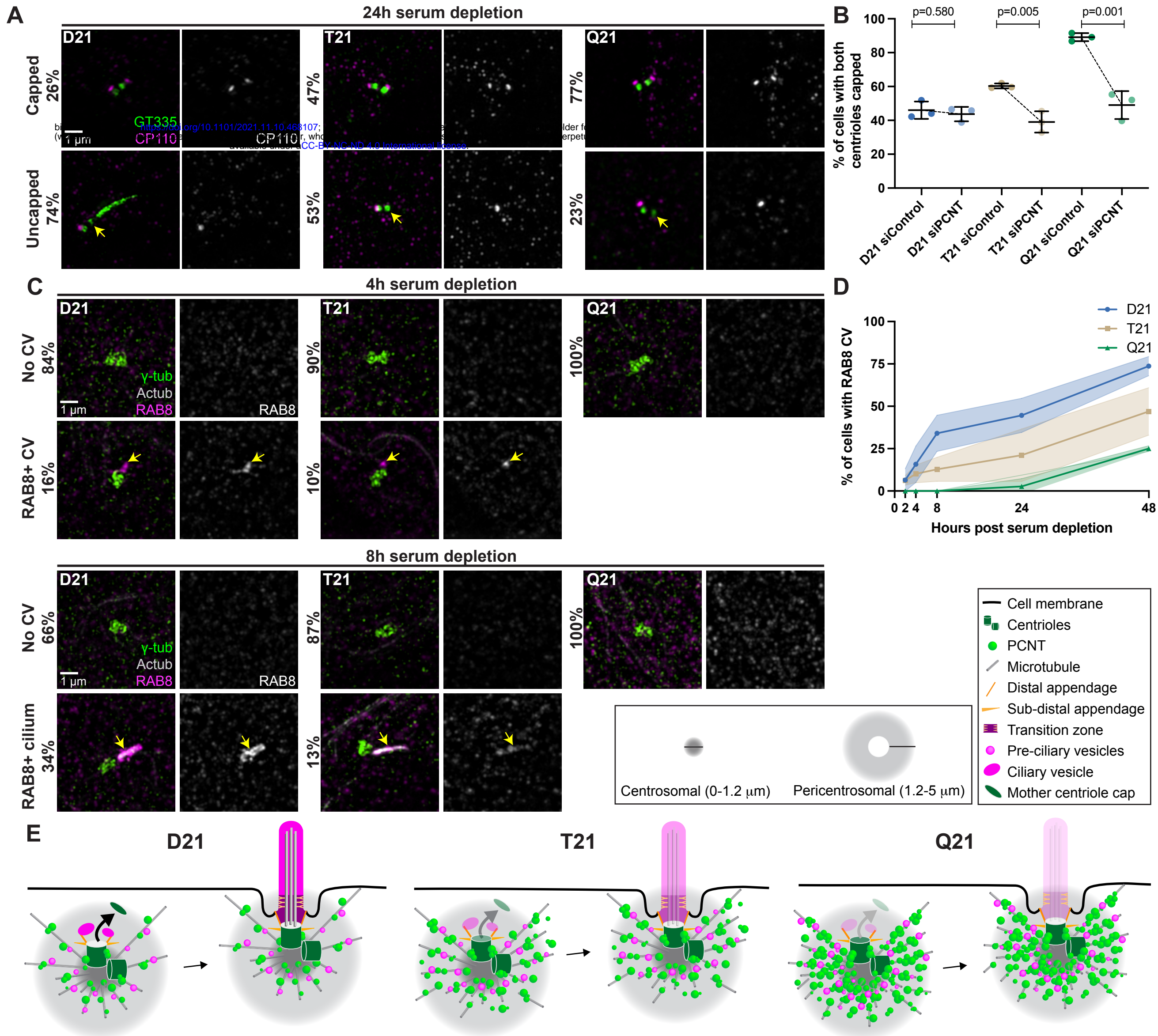


Figure 5

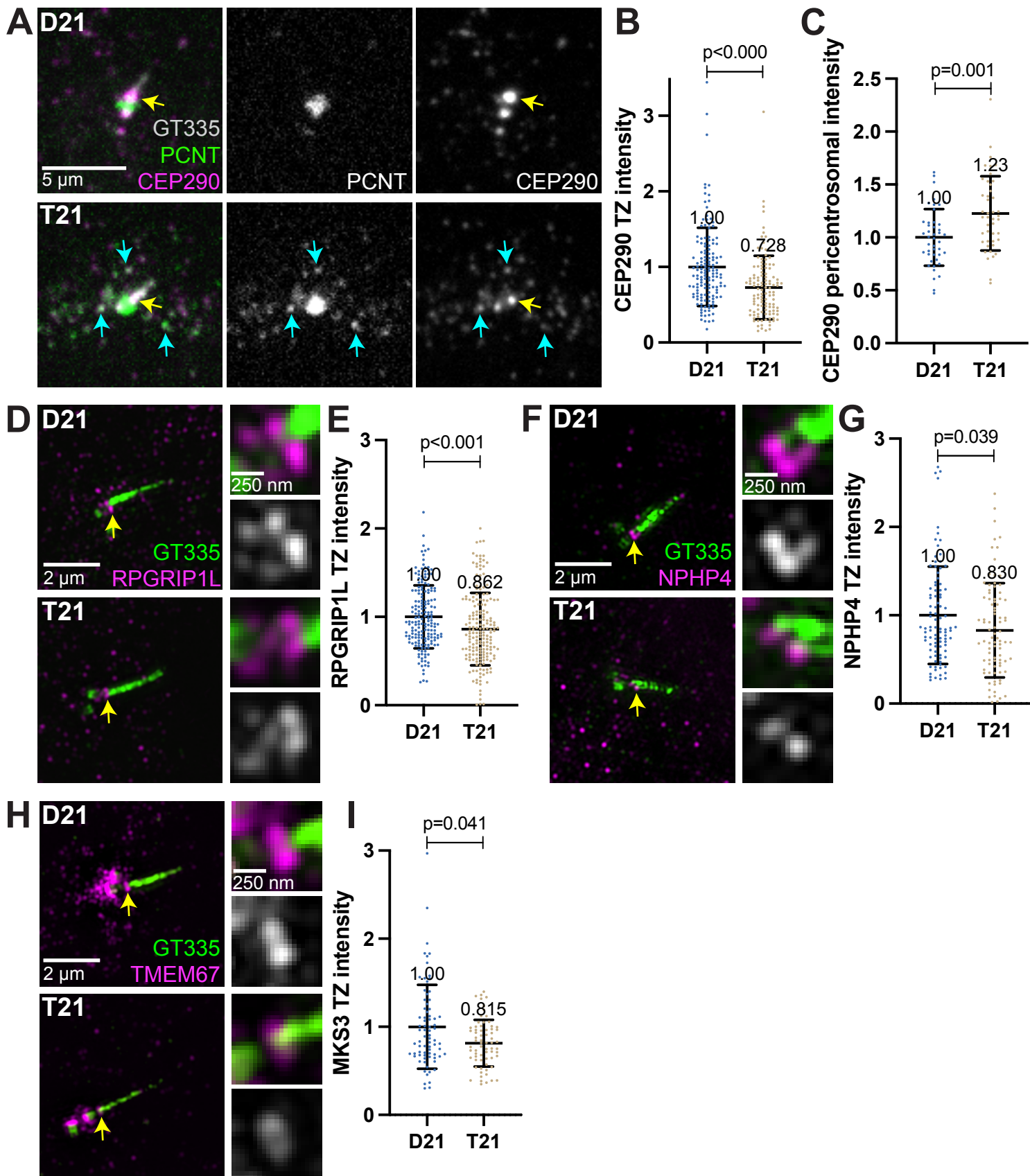


Figure 6

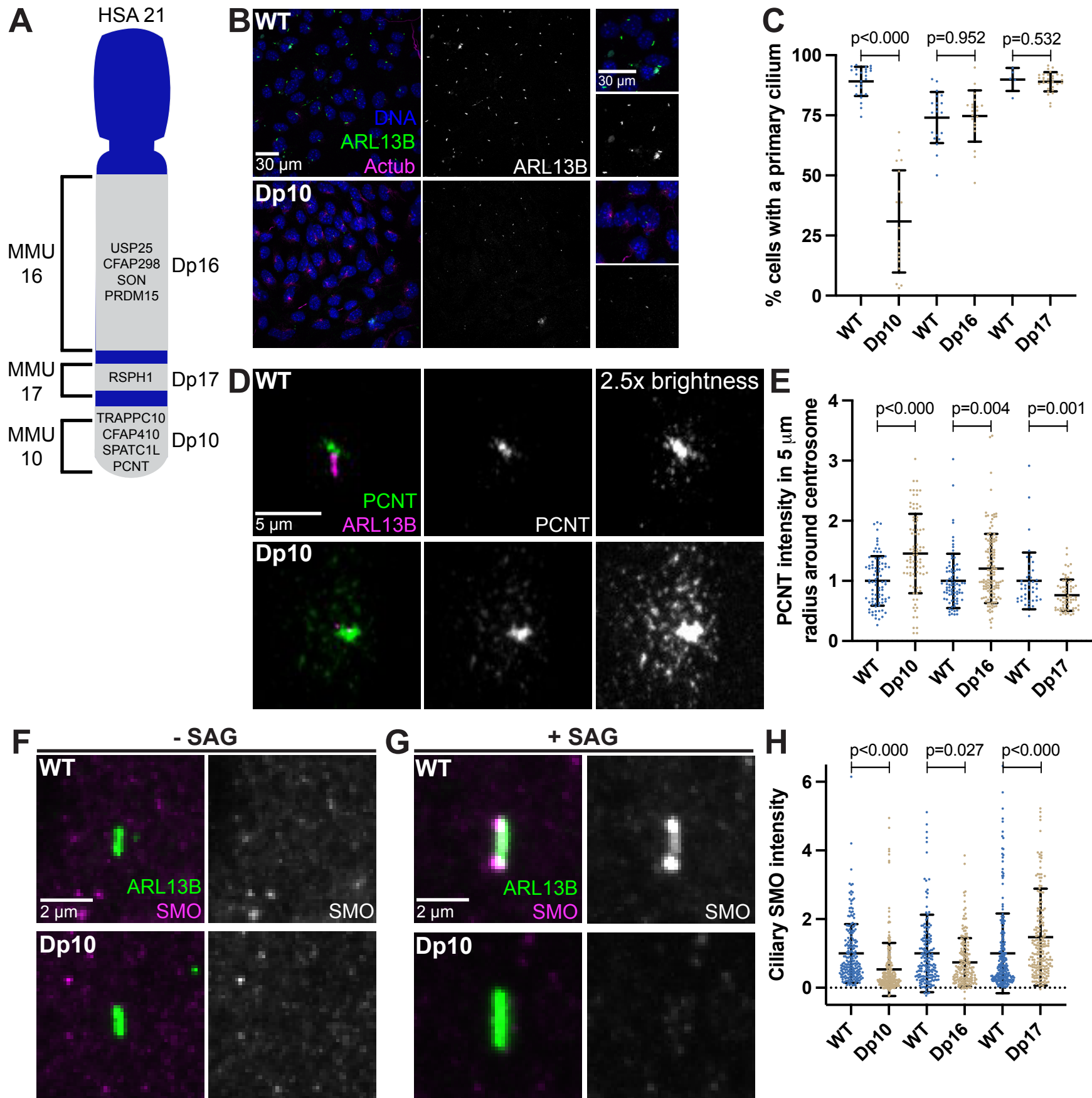
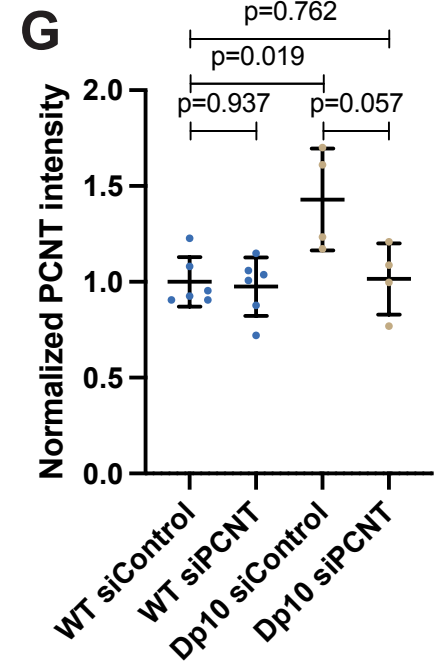
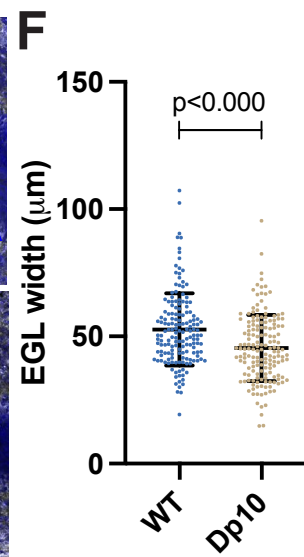
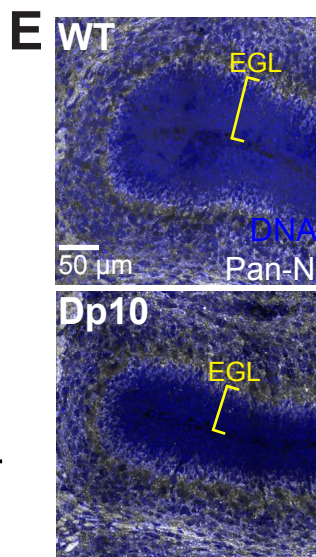
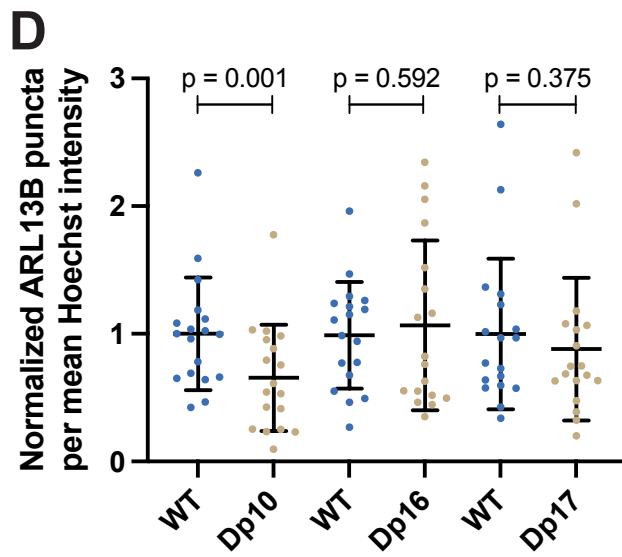
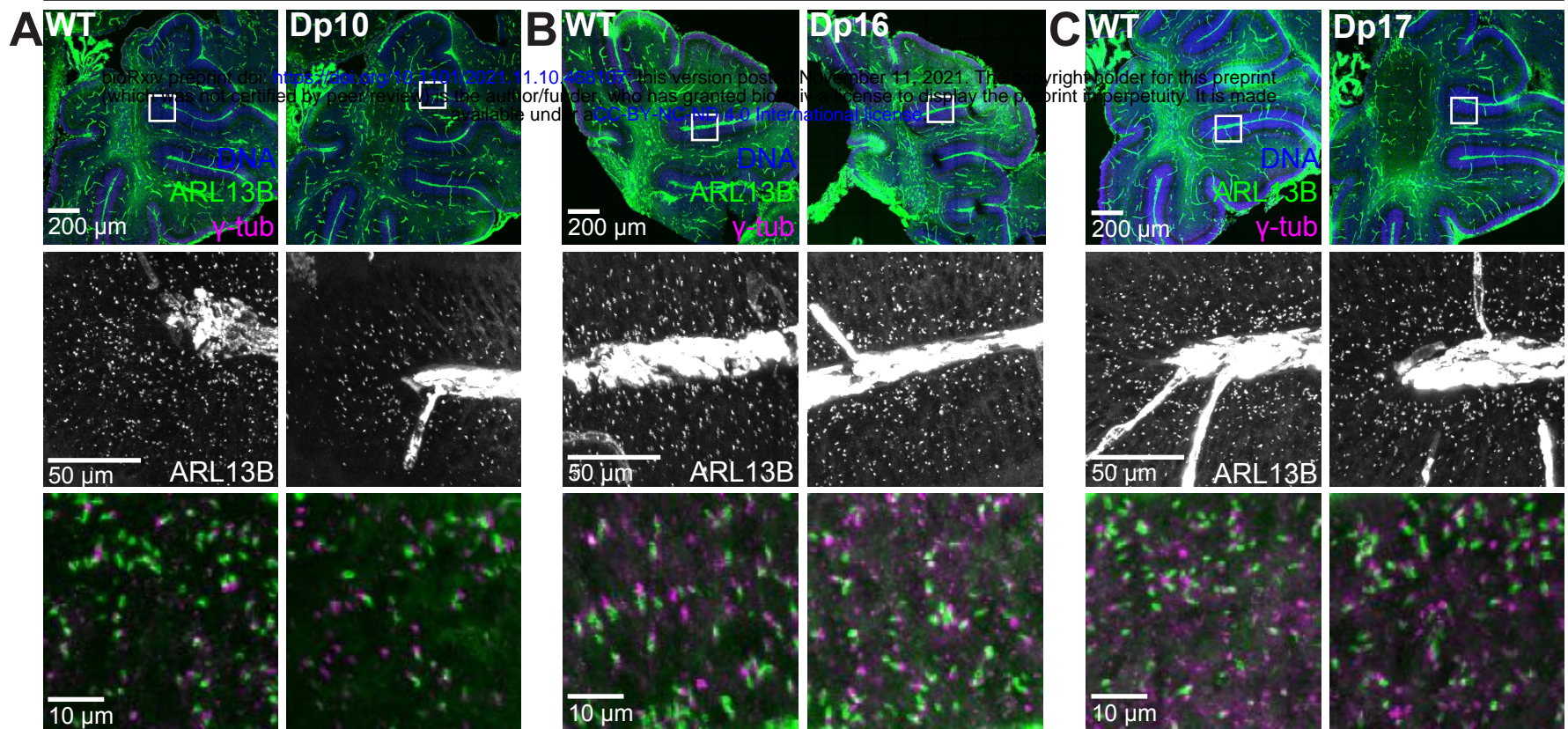


Figure 7

P4 Fixed Sagittal Sections



H Cerebellar Slice Cultures

siControl

siPCNT

